Hochschule für Angewandte Wissenschaften Hamburg
Hamburg University of Applied Sciences

Master Thesis

René Kempe

Sampling pad-electrode configurations with a high density electrode array for transcranial direct current stimulation

Fakultät Life Sciences
Department Medizintechnik

Faculty of Life Sciences
Department of Biomedical Engineering

René Kempe

Sampling pad-electrode configurations with a high density electrode array for transcranial direct current stimulation

Master Thesis eingereicht im Rahmen der Masterprüfung

im Studiengang Master of Science Biomedical Engineering
am Department Medizintechnik
der Fakultät Life Sciences
der Hochschule für Angewandte Wissenschaften Hamburg

Betreuender Prüfer: Prof. Dr.–Ing. Thomas Schiemann
Zweitgutachter: Prof. Lucas C. Parra, Dr. rer. nat.

Eingereicht am: 26. August 2013

Acknowledgements

Deep thanks are owed to my family for supporting me during my studies in Hamburg and New York.

I want to express sincere gratitude to my advisor Lucas C. Parra, who gave me the chance to work on this project, supported me anytime and shared his knowledge and expertise with me.

Also, I want to sincerely thank Thomas Schiemann for the support and trust he gave me while writing this thesis.

Moreover, I would like to give special thanks to Yu Huang, Abhishek Datta and Dennis Truong for helping me with questions regarding this project and doing me many favors during my time in the Neural Engineering Laboratory at the City College of New York.

René Kempe

Title of the thesis

Sampling pad-electrode configurations with a high density electrode array for transcranial direct current stimulation

Keywords

tDCS, brain stimulation, FEM modeling

Abstract

Transcranial Direct Current Stimulation (tDCS) is a non-invasive neuromodulation technology that is under investigation as a treatment for a variety of neurological conditions such as epilepsy, Fibromyalgia, depression, Alzheimer's disease, Parkinson's disease and stroke. Today, sponge-electrode pads are commonly used for current injection in tDCS. Research studies on tDCS often use computational model to provide guidance on the placing of sponge-electrode pads. However, the expertise and computational resources needed for Finite Element Modeling (FEM) makes modeling impractical in a clinical setting. The objective is to make the exploration of different electrode configurations accessible to practitioners by separating it from the computationally demanding process of current flow modeling.

To efficiently estimate current distributions for arbitrary pad configurations pad electrodes are simulated with an array of high-definition (HD) electrodes and an efficient linear superposition is used to then quickly evaluate different electrode configurations. Numerical results on 10 different pad configurations on a normal individual show that electric field intensity simulated with the sampled array deviates from the solutions with pads by only 5% and the locations of peak magnitude fields have a 94% overlap when using a dense array of 336 electrodes. Best results are obtained when assuring complete coverage of the electrode pad with sampled electrodes.

The precise distribution of currents among the HD electrodes is of minor importance, making the uniform distribution an obvious choice. Computationally intensive FEM modeling of the HD array needs to be performed only once. The present results confirm that using these models one can now quickly and accurately explore and select pad-electrode montages to match a particular clinical need.

Contents

List of Figures

List of Tables

1 Introduction

This thesis is based on a project, realized at the Neural Engineering Laboratory of the City College of New York. The core information is submitted for publication in the paper "Sampling pad-electrodes with high-definition arrays for fast and accurate modeling of transcranial electric stimulation" (Journal of Neural Engineering).

1.1 Motivation

Today, new treatment techniques in the fields of biomedical engineering and pharmacology are being developed and improved permanently. They help to provide treatment opportunities of yet untreatable diseases, to reduce side effects and increase patient safety and comfort in already existing therapies and to reduce the costs of medical treatments. The nervous system in the human body is based on electrochemical processes responsible for the generation of action potentials, which represent the actual signals. The corresponding processes can be influenced and modulated by either pharmacological (chemical) means or by the application of electricity to the human body. A well known example is the usage of a cardiac pacemaker to apply electric pulses to the human heart for assuring a continuous and stable heartbeat in patients suffering from cardiac arrhythmia. This project is positioned in the field of electrical stimulation of the human brain, where electrical currents are used to increase or decrease neuronal excitability leading to an alteration of the brain function.

Transcranial direct current stimulation (tDCS) is a non-invasive neurotechnology (still under investigation in clinical studies), which applies small constant currents (ranging from 0.2 mA to 2 mA) to the surface of the scalp to achieve neural modulation [1, 2]. To estimate current distributions in the brain and to select a proper pad configuration, high-resolution computational models of the human head are often

used in clinical research. Individual anatomy varies significantly across patients due to the intricate folding of the cortical surface, varying skull thickness and distribution of cerebrospinal fluid (CSF). These variations can have a large effect on the current flow inside the head [3, 4]. To include these details it is important to use anatomical head models of at least 1 mm resolution. Unfortunately, the resulting models for the finite element method (FEM), which are conventionally used for these numerical simulations, require substantial computation time and memory usage (about 2 hours for placing the pad electrodes on the model, 2 hours for the mesh generation and 1 hour for the FEM calculation for a single solution [1] [6, 7]. This is a problem regardless of the specific modeling choice (anisotropy, number of tissues modeled, etc). Fast modeling solutions that have been proposed to-date do not include CSF or detailed cortical folding [8]. Thus, solutions with the required spatial resolution are not practical for routine clinical use [9].

This thesis demonstrates the possibility to sample pads with a subset of high-definition (HD) electrodes that can be solved in advance. With this approach a given pad can be quickly simulated as the sum of preexisting solutions computed with high spatial resolution. The simulation of the pad is then based on an efficient linear superposition of these individual solutions, which can be readily evaluated for different configurations. The present objective is to make the process of exploring different electrode configurations more efficient by separating it from the computationally demanding FEM modeling. A comparison of the proposed method with models of continuous pad-electrodes shows only a small discrepancy in field intensity and peak magnitude locations – comparable to what may be observed with other modeling choices or resulting from small tissue segmentation errors [7].

FEM modeling of the HD array needs to be performed only once, while clinical researchers and practitioners can then use these solutions to explore and select pad-electrode montages depending of their specific clinical target. In the future, when automated segmentation and modeling becomes more routine these precomputed solutions could also be generated for individual patients so that practitioners may adjust electrode placement for individual subjects.

[1] using a PC with Intel® Quad Core Xeon® W5580 CPU at 3.2 GHz and 96GB RAM

1.2 tDCS

1.2.1 History

tDCS is based on the principle of using direct current for stimulation, which is around for quite some time. In 1780 for example, Luigi Galvani noticed the contraction of frog legs by current injection. Mid of the 19th century, Emil Heinrich Du Bois-Reymond proved the contraction of muscles by electrical oscillation. Some years later Gustav Theodor Fritsch and Eduard Hitzig showed the electrical excitability of the cerebrum by current injection to a dog's brain leading to eye movement.

Since the 1960s, DC stimulation again was used frequently in animal experiments. Brain stimulation on rats showed a persistent increase or inhibition of the cortical excitability. Also the different effects of using either positive or negative stimulation were discovered. Nevertheless in the following years research in this field was again dropped since more effective and easier therapy methods, i.e. drug therapy, were developed. With the beginning of the 20th century, tDCS was "rediscovered", driven by a better understanding of the brain function and stimulation and imaging techniques, like transcranial magnetic stimulation (TMS) and functional magnetic resonance imaging (fMRI).

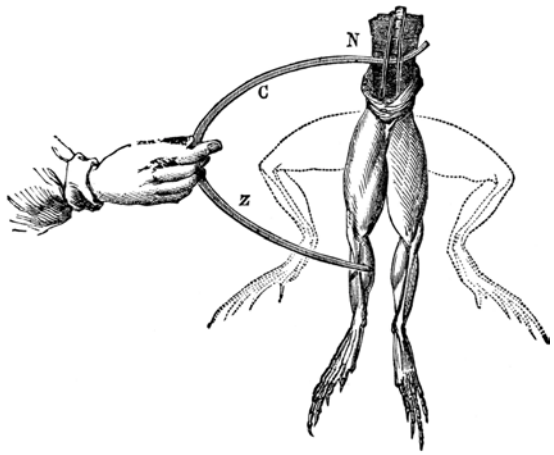

Figure 1.1: "Galvani found that whenever the nerves of a frog's leg were touched by one metal and the muscles by another, convulsions took place on bringing the two different metals in contact." –Wells, 1857 [10]

Today, tDCS is frequently used in clinical studies on therapies that help improving neurological disorders. The major advantage of tDCS is the relatively safe, non-invasive and cheap application.

1.2.2 Application

tDCS has shown promise in treatment for neurological disorders such as epilepsy [11], Fibromyalgia [12], depression [13], Alzheimer's disease [14], Parkinson's disease [15] and stroke [16, 17, 18]. It has also been shown to improve cognitive functions, like memory and learning in healthy individuals [19]. Some study examples:

1. In an epilepsy study tDCS was used in 19 patients [11]. Cathodal stimulation was applied to the area, causing refractory epileptic activity, aiming to decrease cortical excitability. The authors state that "Active compared with sham DC polarization was associated with a significant reduction in the number of epileptiform discharges" and also that "the results suggest that this technique might have an antiepileptic effect based on clinical and electrophysiological criteria".

2. Another study with 32 patients suffering from Fibromyalgia was conducted [12]. In this case tDCS was used to test for positive effects on chronic muscle and tissue pain related to Fibromyalgia. Stimulating the motor cortex led to "a larger, significant improvement of pain compared with sham stimulation. This effect is specific to the site of stimulation and can last for several weeks after treatment with stimulation has ended".

3. Anodal tDCS was used for a study on stroke patients suffering from post-stroke paresis [17]. Having stimulated a "hand-associated" motor cortex area, a significant (compared to sham-stimulation) motor function improvement of the right paretic hand was observed. The comparison was based on a widely accepted motor function test with everyday challenges for paretic patients like turning cards or picking up beans with a spoon. An improved motor function was detected in every tDCS patient. As a result it was supposed that tDCS may have positive effects on the motor function in post-stroke paretic patients.

1.2.3 Technique

Aiming to polarize brain tissue electrically to modulate the brain activity of specific areas, during tDCS a constant, low direct current is sent through the electrodes. Having placed these electrodes at the region of interest, the current induces intracerebral current flow. This current flow can either increase or decrease the neuronal excitability in that specific area. Changing the neuronal excitability leads to an alteration of the brain function, which can be useful for various therapies.

For the application of tDCS only a few parts are necessary, i.e. at least two electrodes (Figure 1.2) and a battery powered device delivering constant current (Figure 1.3). Additionally, a control software can be used, f.e. to provide settings for blinding in experimental studies or to restrict the total amount injected current. Each device has a positively charged, anodal and a negatively charged, cathodal electrode. The electrical current flows from the cathode through the skull and brain to the anode, creating a circuit. The current delivering device has controls to set the current and the duration of stimulation. Also the size of the electrodes differs, smaller sized electrodes can achieve a more focused stimulation while a larger electrode ensures that the whole region of interest is stimulated.

(a) (b)

Figure 1.2: Application of tDCS with (a) pad electrodes and (b) HD electrodes.

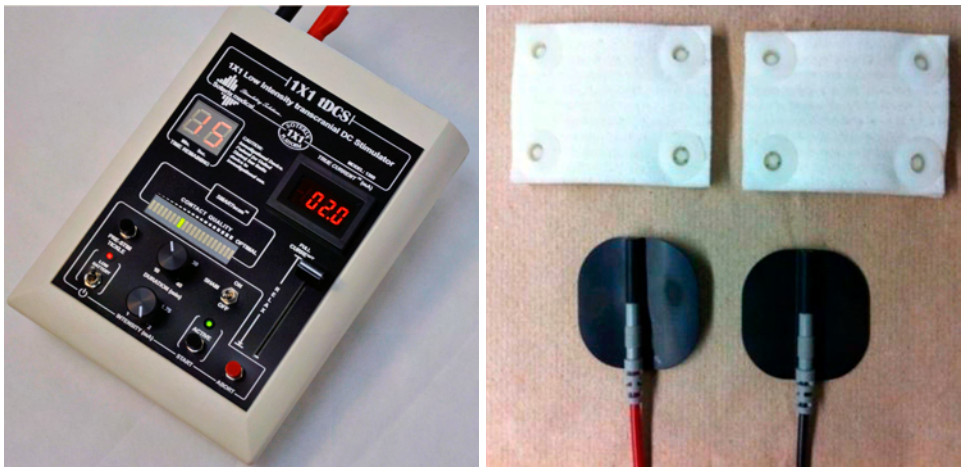

(a) (b)

Figure 1.3: (a) tDCS device (Soterix Medical) and (b) pad-electrodes with sponges.

There are three different stimulation types: anodal, cathodal and sham stimulation. While the positive, anodal stimulation increases, the negative, cathodal stimulation decreases the neuronal excitability of the targeted area. Cathodal stimulation can be used to treat psychological disorders caused by the hyper-activity of a certain brain region. Sham stimulation is generally used to control experiments, where current will only be ramped up for a short time at the beginning and the end of the tDCS session. That way a tingling skin sensation can be achieved to make the patient believe that he is actually being stimulated. Thus sham is used to test whether the effects of the real tDCS are significantly stronger than possible placebo effects.

1.3 Modeling and tDCS simulation

Many clinical trials in the field of tDCS are guided by high resolution MRI-derived FEM models. Latest models have evolved from previous models with simplified geometries. Initially, concentric sphere models were developed to examine the role of various electrode configurations. First MRI-derived human geometry was introduced by Wagner et al. [20]. Gyri-precise modeling was then developed by Datta et al. [3], allowing to predict the field distribution for specific brain regions.

Today, the used models are MRI-derived finite element models with subject specific anatomy (1.4a). A brief overview of the process, described in more detail in Chapter 2: High resolution MRIs are segmented into different tissue masks of corresponding conductivities by a combination of automated scripts and manual labor. Computer generated models of electrodes and gel are incorporated into the segmentation. Afterwards volume meshes are generated, boundary conditions applied and the Laplace equation is solved (see Section 2.2 for more details). The resulting cortical electric field is interpreted as a correlate for stimulation and modulation (Figure 1.4b).

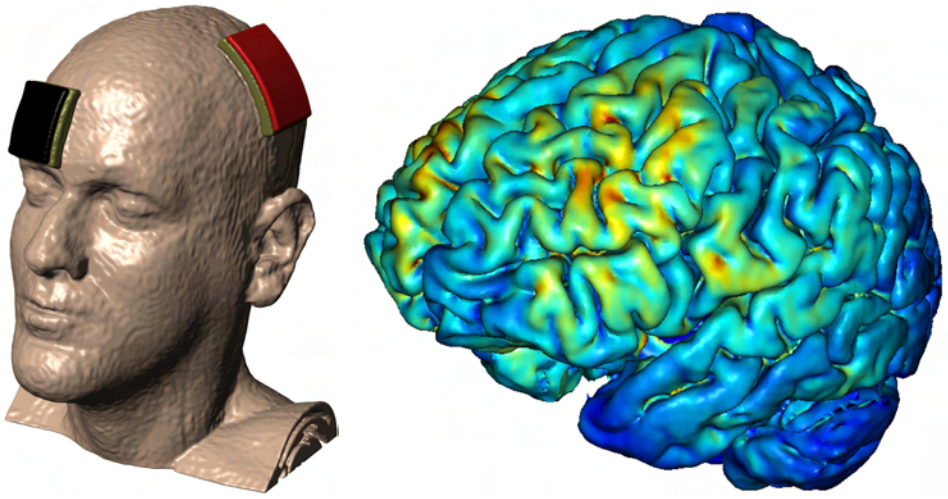

(a) (b)

Figure 1.4: (a) Model with the specific pad-electrode configuration M1-SO (motor cortex stimulation) and (b) the corresponding simulation of the electric field distribution.

For better handling and inspection of these models, software tools have been developed (f.e. HDExplore by Soterix Medical Inc.[2], Figure 1.5). Here the user can choose a number of HD electrodes, set the corresponding stimulation currents and inspect the field distribution inside of the brain.

But it is not only possible to simulate the electric field distribution inside of the head for a given electrode setup. The Software HDTargets (Soterix Medical Inc.) allows the user to select a target area and subsequently determines the optimal HD electrodes configuration for that specific stimulation.

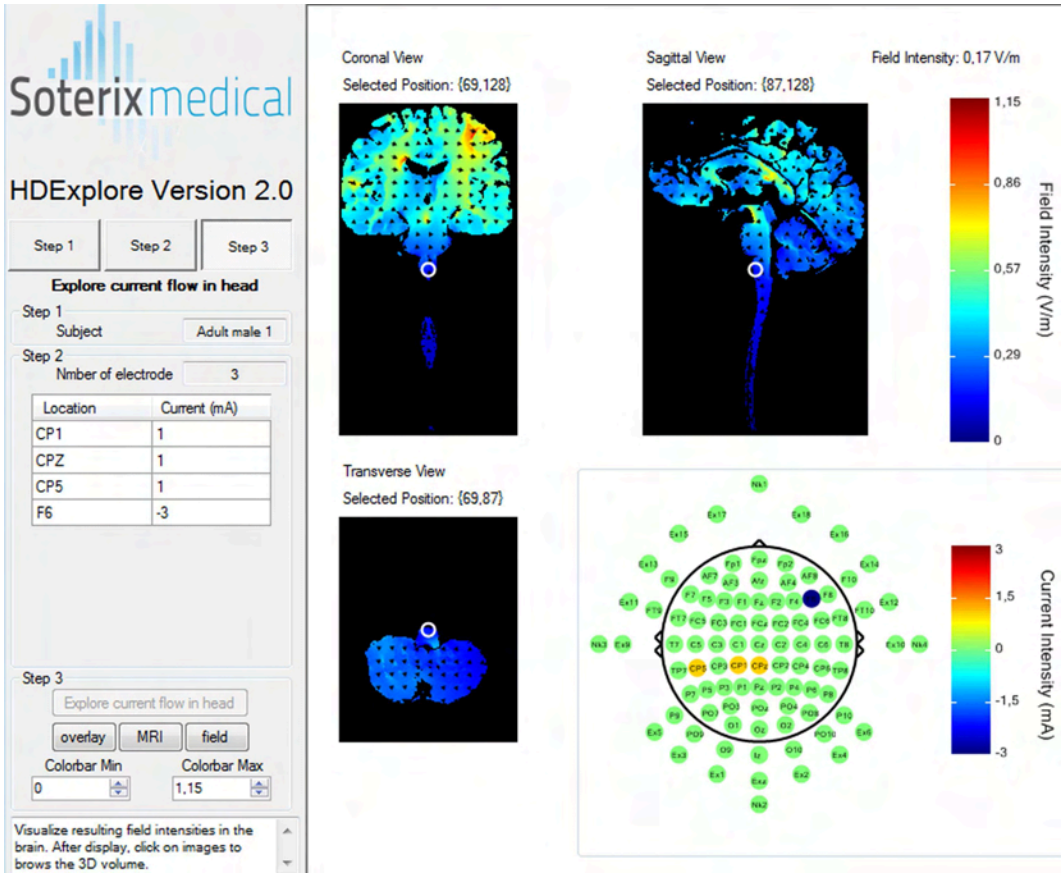

Figure 1.5: Software HDExplore (Soterix Medical) used to simulate the field distribution of 92 HD electrodes.

[2] http://www.soterixmedical.com

2 Methods and approach

In this chapter the subsequent steps of model generation, FEM calculation, data processing and analysis are described. The basic process of this pipeline is illustrated in Figure 2.1.

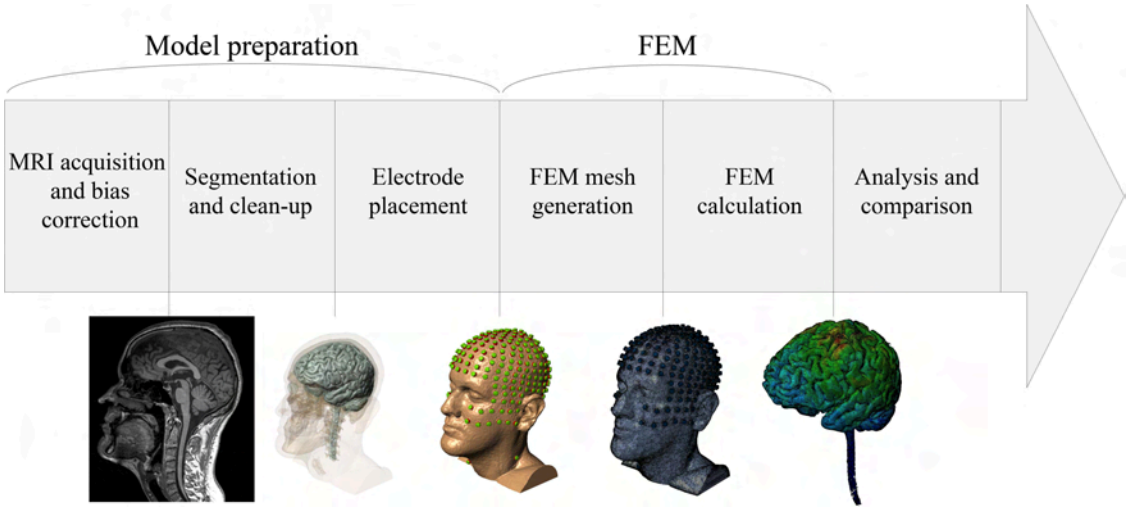

Figure 2.1: Workflow for individualized tDCS modeling.

2.1 Model preparation

The basis of creating the human head model is an MRI-data set. Once the MRI is obtained, it is segmented into different tissue types which is necessary to specify the corresponding electric conductivity for each tissue. After automated segmentation and subsequent segmentation error clean-up, the electrodes are placed on the head. Then the model can be used for computation.

2.1.1 MRI segmentation and clean-up

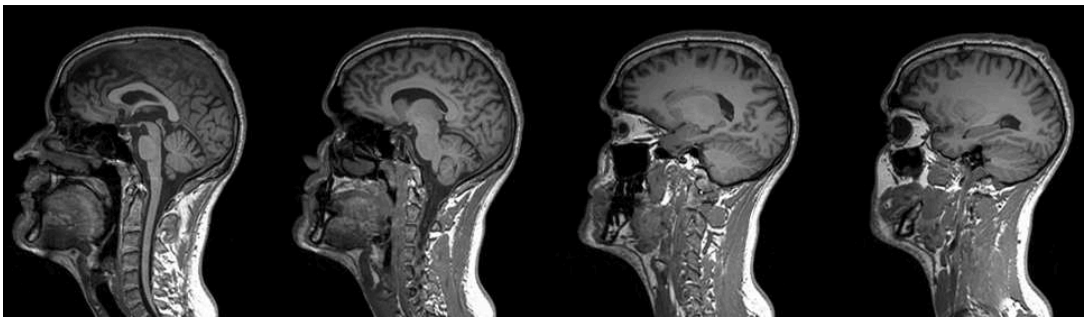

Figure 2.2: MRI-data set (selected slices) used for model generation.

The head model was derived starting from a T1-weighted MRI scan from a healthy subject (male, 36 years old) (Figure 2.2). First, automated segmentation was performed using SPM8 (SPM8, Wellcome Trust Centre for Neuroimaging, London, UK) to demarcate the MRI image into six categories: skin, skull bone, CSF, gray matter (GM), white matter (WM), and air. Because of image noise and some low contrast areas, errors like discontinuities and unconnected voxels occurred (Figures 2.3a, 2.4a). An in-house MATLAB (Mathworks, Natick, MA) script [7], using morphological and Boolean operators, was used to correct the automatic segmentation errors (Figures 2.3b, 2.4b). Residual segmentation errors were finally fixed manually in ScanIP (Simpleware, Exeter, UK) (Figures 2.3c, 2.4c and 2.5).

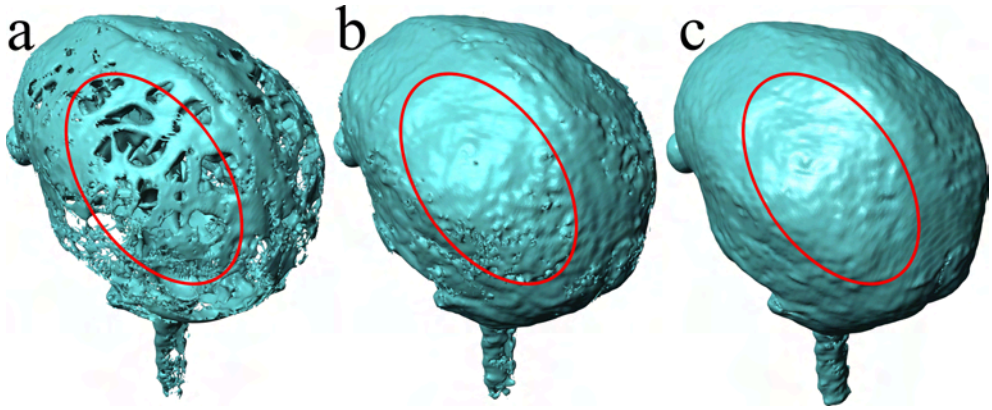

Figure 2.3: Errors in the CSF segmentation: (a) discontinuities after automated segmentation, (b) improvements after automated clean-up and (c) final result after manual fixes.

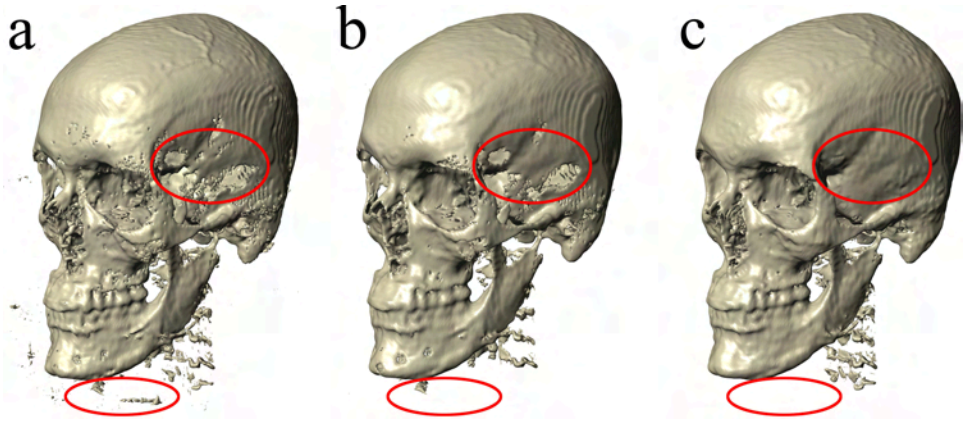

Figure 2.4: Errors in the bone segmentation: (a) discontinuities and unconnected voxels, (b) improvements after automated clean-up and (c) final result after manual fixes.

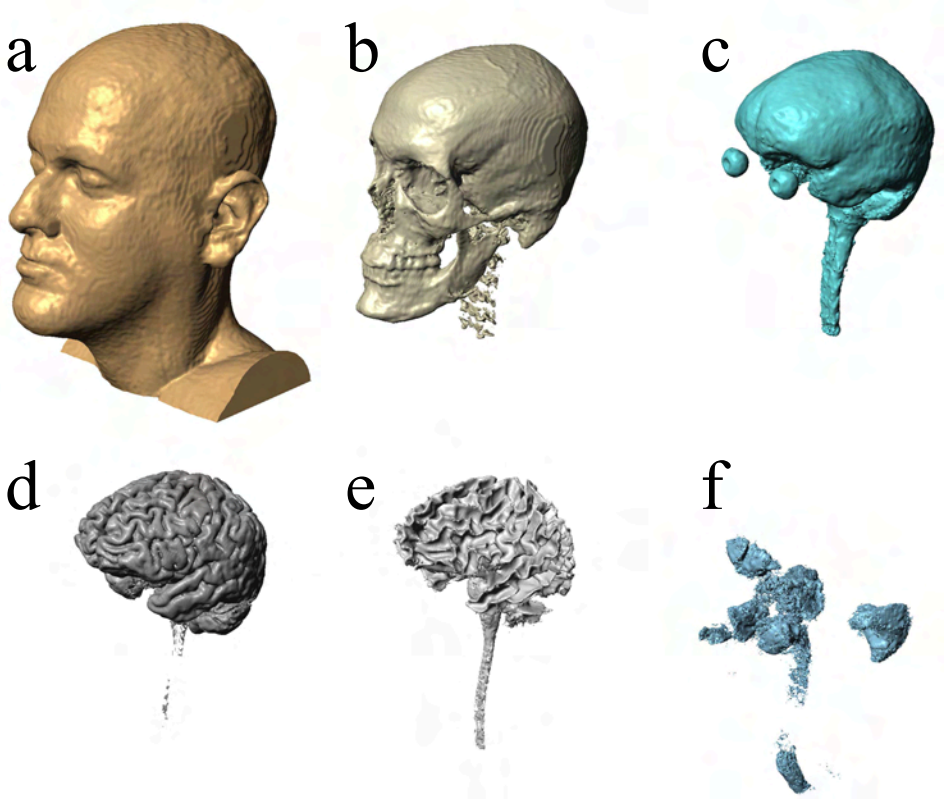

Figure 2.5: Final segmentation masks from (a) to (f): scalp, skull, CSF, GM, WM and air.

2.1.2 Electrode placement

Before placing the electrodes on the scalp, the decision for an electrode positioning system (based on EEG configuration standard) had to be made. It is important to use a system with a high number of electrodes to be able to sample the pad-electrodes as good as possible, meaning a sufficient sampling coverage (see Section 3.1.3). For the same reason also the distribution of electrodes on the head should be uniform. The following systems were under consideration:

10-5 system

Based on the international 10-10 system with 74 electrodes, which itself is an extension of the 10-20 system (21 electrodes), a model with 329 electrodes was generated. Unfortunately some of the electrodes are too close towards each other leading to overlaps.

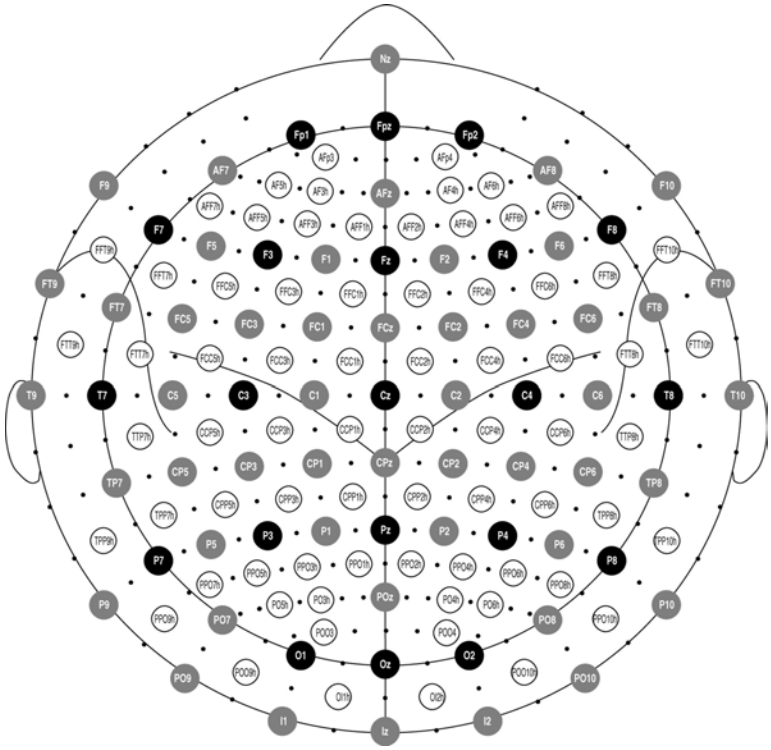

Figure 2.6: Schematic of the 10-5 system [21].

Geodesic system

Another way to place the electrodes is based on geodesic system. But it turns out that the electrodes in general are not dense enough in some areas caused by the lower number of electrodes (256) and their non-uniform distribution (Figure 2.9b).

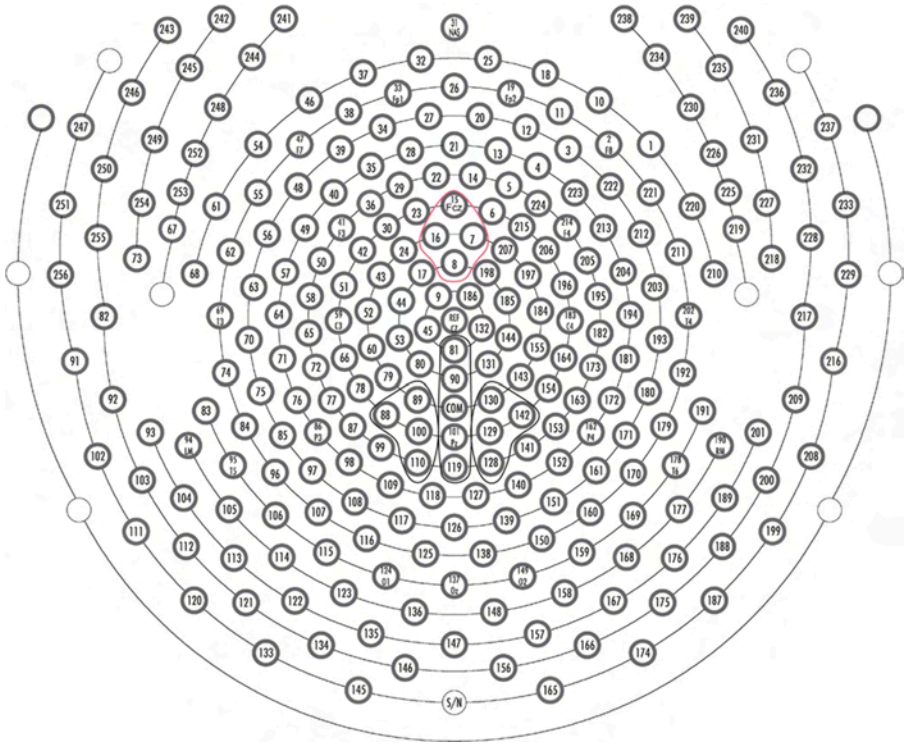

Figure 2.7: Schematic of the geodesic system [22].

Concentric system

The concentric system (after extension) uses 336 electrodes. The decision was made to implement the concentric system as it offers a dense and uniform electrode distribution, which allows a good sampling of the pad-electrodes (Figure 2.9c).

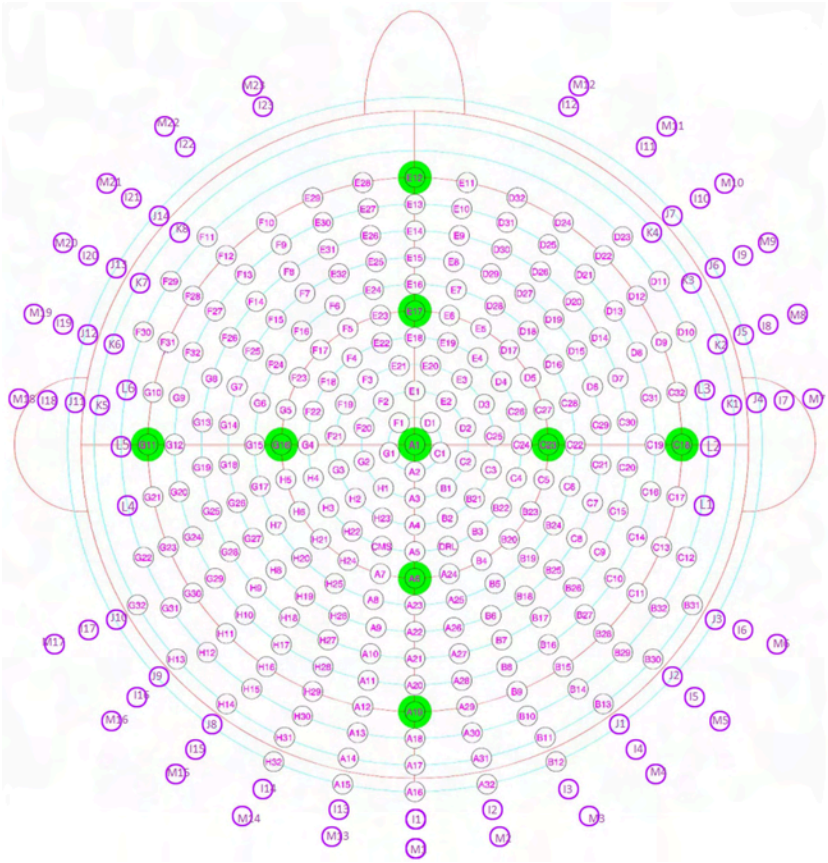

Figure 2.8: Schematic of the concentric system.

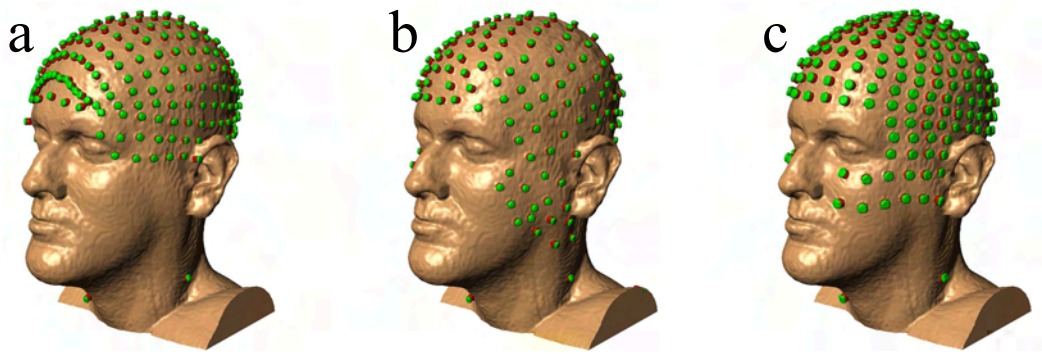

Figure 2.9: Models with the described electrode placement systems: (a) 10-5 system, (b) geodesic system and (c) concentric system.

The small electrodes (4 mm radius to prevent overlap) were placed automatically on 336 locations on the scalp using a MATLAB script [7]. The montage follows the conventional concentric system with 258 electrodes by BioSemi (BioSemi B.V., Amsterdam, Netherlands) with additional electrodes.

Further rows of electrodes were placed to potentially allow stimulation of deeper or lower-lying cortical targets (compare Figure 2.14a). Also four additional electrodes were placed around the neck which may serve to emulate distant reference electrodes. In total this adds up to 336 electrodes (258 in original concentric system + 74 in additional rows + 4 neck electrodes). After generating the six tissue masks and two masks for electrodes and gel, a complete model of the head was created Figure 2.10).

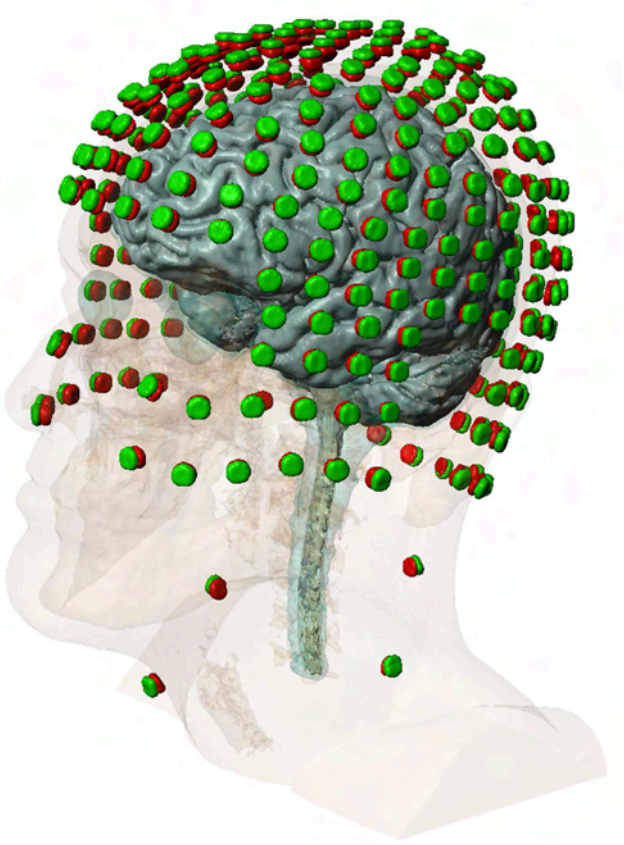

Figure 2.10: Final model with concentric electrode placement (transparent scalp and skull masks for visualization of the brain covered by the electrodes (green) and gel (red)).

2.2 FEM

Before conducting an FEM calculation, it is necessary to discretize the model into single elements. Therefore one typically makes use of specific software for FEM mesh generation. After generating the mesh it can be further processed in an FEM computation software. Once the boundary conditions and initial statii are set, the FEM calculation can be performed. Creation and solving of the FEM model followed existing procedures [7, 23].

2.2.1 Mesh generation

Meshing with ScanIP

ScanIP was used to generate a mesh with tetrahedral elements applying adaptive meshing to limit the size of the total model. This algorithm chooses the size of each element adaptively based on the detail level in the structure. This way, small structures requiring a 1 mm resolution are properly meshed. Other, less detailed and uniform regions can be represented by bigger tetrahedral elements, saving time at the mesh generation process. The meshing process took about 2 hours for the whole model resulting in approximately 8.5 million elements and 1.5 million nodes with about 12 million degrees of freedom.

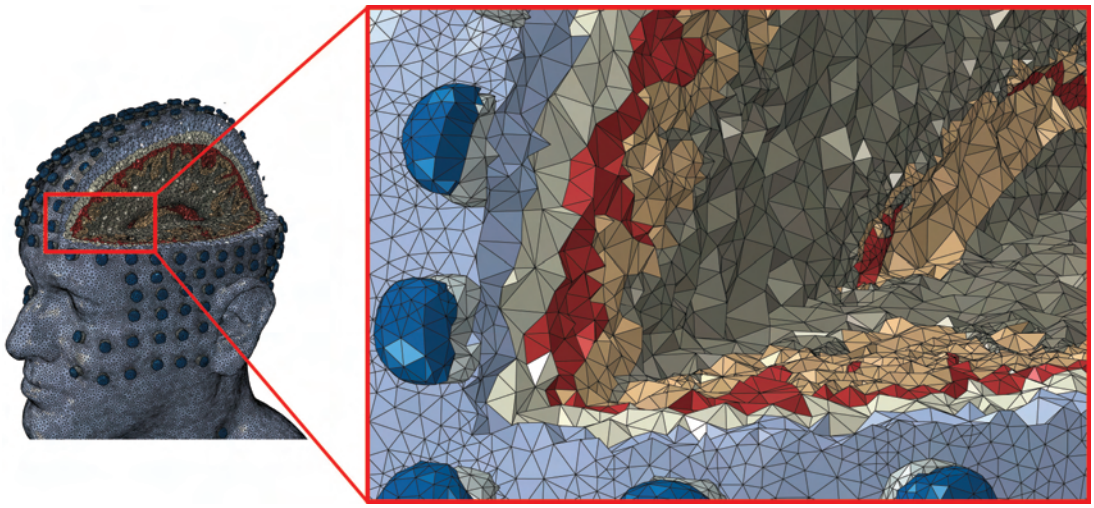

Figure 2.11: Result of the meshing using ScanIP (detail shows the adaptive mesh).

Alternative meshing approaches

As one always tries to make use of free Software, it was considered to replace ScanIP with a freeware tool to generate the meshes. Besides other commercial solutions like Mimics[1] or Amira[2], meshes have also been generated with the freewares Tetgen[3] and Iso2Mesh[4]. Fastest promising results among the freeware tools were accomplished using Iso2Mesh, which may serve as an alternative in the future. It also offers different parameters, controlling the detail level. A simple trial showed that the meshes, generated with Iso2Mesh can be processed the same way as ScanIP output and lead to similar FEM results at first sight.

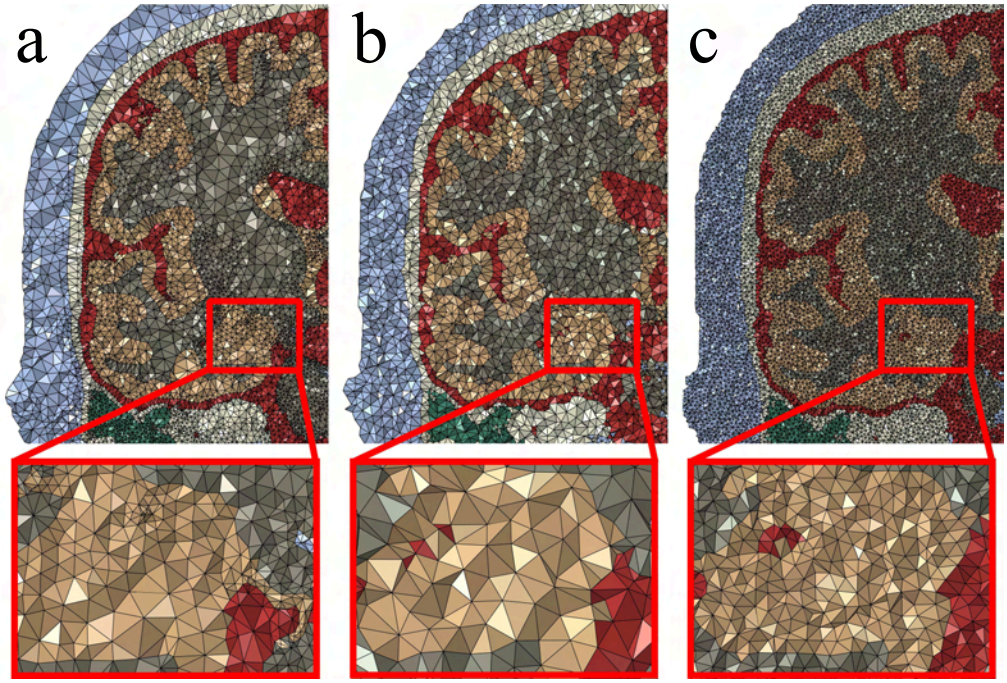

Figure 2.12: Visual comparison of the different meshing approaches using (a) ScanIP with adaptive meshing, (b) Iso2Mesh with detail parameter 200 and (c) Iso2Mesh with parameter 1500. The meshes created with Iso2Mesh clearly do not use any kind of adaptive meshing, leading to either a lower resolution (b) or a high resolution over all regions resulting in a higher computation time (c).

[1] http://biomedical.materialise.com/mimics
[2] http://www.vsg3d.com/amira
[3] tetgen.berlios.de
[4] http://iso2mesh.sourceforge.net/cgi-bin/index.cgi

2.2.2 FEM calculation

To model the current flow the head is assumed as a volume conductor comprised of distinct tissues with a specific, uniform (assuming isotropic) conductivity.

The current density $\mathbf{J}$ in the volume should have zero divergence, since there are no current sources inside of the head: $\boldsymbol{\nabla} \cdot \mathbf{J} = \boldsymbol{\nabla} \cdot (\sigma \mathbf{E}) = 0$, where $\boldsymbol{\nabla}$ is gradient operator ($[\frac{\partial}{\partial x}, \frac{\partial}{\partial y}, \frac{\partial}{\partial z}]$), σ is the conductivity and $\mathbf{E}$ is the electric field in the volume. When current passes from anode to cathode, the resulting electric potential distribution V in the volume satisfies Laplace's Equation:

$$\boldsymbol{\nabla} \cdot \mathbf{J} = \boldsymbol{\nabla} \cdot (\sigma \mathbf{E}) = -\boldsymbol{\nabla} \cdot (\sigma \boldsymbol{\nabla} V) = 0 \tag{2.1}$$

Assuming $\mathbf{E}$ (or equivalently $\mathbf{J}$) being continuous at tissue boundaries where the conductivity changes, and if $\mathbf{E}$ is specified at the outer boundary of the volume (the boundary conditions), the solution to Laplace's Equation is unique.

For arbitrary shaped media, no closed form solution exists and one typically uses numerical techniques. Therefore, the volume is discretized into a set of finite elements with uniform conductivity, and Laplace's Equation is solved at all elements.

Calculation with Abaqus

The FEM calculation was performed with Abaqus (Simulia, Providence, RI) using automated batch-processing scripts. The standard Laplace equation was solved with conjugate gradients iterative solver. For each of the 336 HD electrodes, the applied current was set to 1 A/m^2 at the anode electrode and ground was applied at a common reference electrode. For solving the model, following boundary conditions were used:

- Electric insulation for all outer boundaries: $\mathbf{n} \cdot \mathbf{J} = 0$;
- Continuity for inner boundaries: $\mathbf{n} \cdot (\mathbf{J_1} - \mathbf{J_2}) = 0$;
- Inward current flow for anode: $-\mathbf{n} \cdot \mathbf{J} = J_n$;
- Ground for cathode(s): $V = 0$;

where $\mathbf{n}$ is the normal vector of the boundaries, $\mathbf{J_1}$ and $\mathbf{J_2}$ are current densities in two different tissues, J_n is the magnitude of the applied current and each tissue type was assigned a conductivity value according to Table 2.1.

Table 2.1: Different tissue types with corresponding conductivity

tissue	**conductivity** (S/m)
grey matter	0.276
white matter	0.126
CSF	1.65
bone (skull)	0.01
skin (scalp)	0.465
air	2.5×10^{-14}
gel	0.3
electrode	5.9×10^{7}

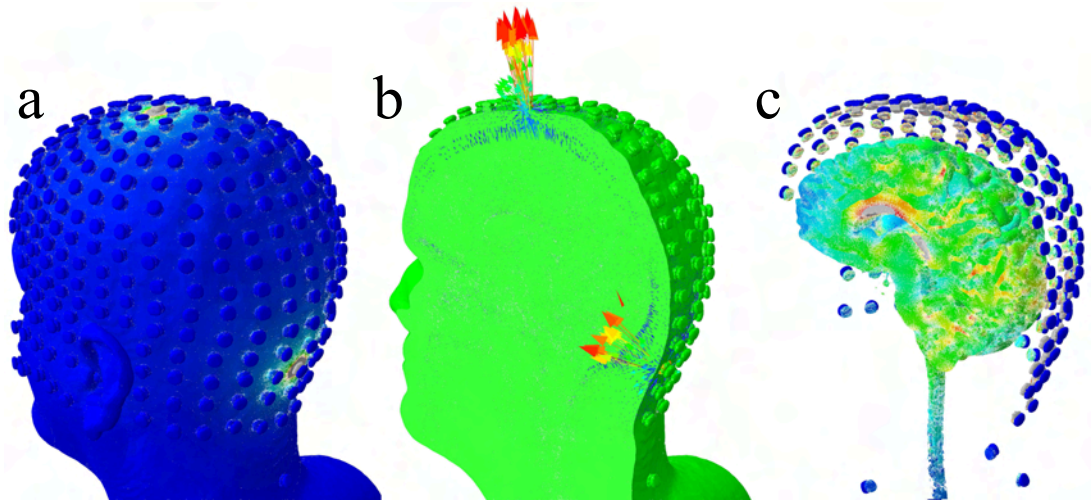

Figure 2.13: Visualization of a single FEM result. (a) Electric field distribution on the scalp, (b) current direction and (c) field distribution inside of the brain.

The process of running Abaqus was automated by executing the Abaqus console application for each of the 336 electrodes via a Matlab script. The calculation for one pair of electrodes takes about 1 hour. Once the FEM equations were solved the solution files for all electrodes were saved. This file contains a list of mesh nodes with the corresponding xyz-coordinates and the electric potential gradient. The Abaqus solutions on the tetrahedral grid were read back into MATLAB and interpolated on the original 3D regular grid of the MRI segmentation.

2.3 Pad sampling and electrode weighting

After finishing the FEM calculations for each electrode, the solution files need to be further processed.

2.3.1 Sampling process

For the subsequent error calculation and comparison, 10 standard pad configurations were also solved (Figure 2.14b and A.1, A.2, A.3). Pad-electrodes were constructed with ScanCAD. The pad-electrodes were placed manually on the scalp at commonly used locations using ScanIP, and FEM computation as well as current scaling (Subsection 2.3.2) was performed identical to the HD electrodes model.

a

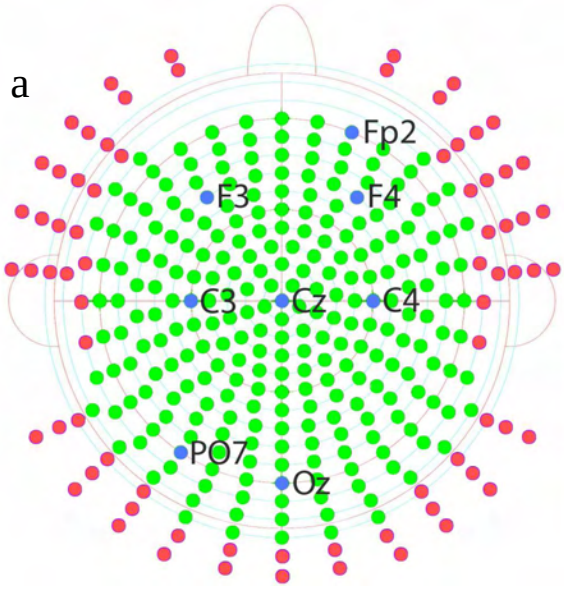

b

#	pad configurations	pad sizes	# of electrodes
1	Cz-F4	5x5 - 5x5cm²	10-10
2	C3-C4	5x5 - 5x5cm²	9-11
3	F3-F4	5x5 - 5x5cm²	9-10
4	Oz-F4	5x5 - 5x5cm²	9-10
5	C4-F4	5x5 - 5x5cm²	11-10
6	F3-C4	5x5 - 5x5cm²	10-11
7	Oz-Cz	5x7 - 5x7cm²	9-13
8	PO7-F3	5x5 - 5x5cm²	12-9
9	PO7-F4	5x5 - 5x5cm²	12-10
10	Oz-Fp2	5x5 - 5x5cm²	9-9

Figure 2.14: (a) Two dimensional schematic of the arrangement of scalp electrodes. 74 electrodes (red) were added to the concentric system provided by BioSemi (258 green electrodes). 4 additional neck electrodes are not displayed. Blue circles indicate the locations (according to the 10-10-system) of electrodes representing regions of the sampled pad configurations. (b) List of pad configurations used including their sizes and the number of electrodes used to sample these pads (anode-cathode).

The selection of the considered pad configurations, including varying pad sizes, is based on previous clinical use for the configurations C3-C4 [24], F3-F4 [13], Oz-Cz [25] as well as arbitrary combinations of other locations to quantify the possible variability in the results.

Notice that the size of the pad electrodes for the Oz-Cz configuration differs from the other configurations. With this the sampling technique for another pad size can be analyzed, i.e. a rectangular pad of 5×7 cm^2, instead of only quadratic, 5×5 cm^2 pads. The specific choice was based on previous modeling studies that used those dimensions [25].

Subsequently, these solutions were approximated by sampling the pad with the small HD electrodes, i.e. the sampled solutions are a linear superposition of the solutions of the subset of HD electrodes overlapping in location with the pad-electrode. Thus, a simple addition (negligible computation time) of all HD electrodes solutions, used to sample the pad, leads to the simulation of the continuous pad-electrode. An electrode was included in the sampling subset if at least half of its area was covered by the pad's area (Figure 2.15c).

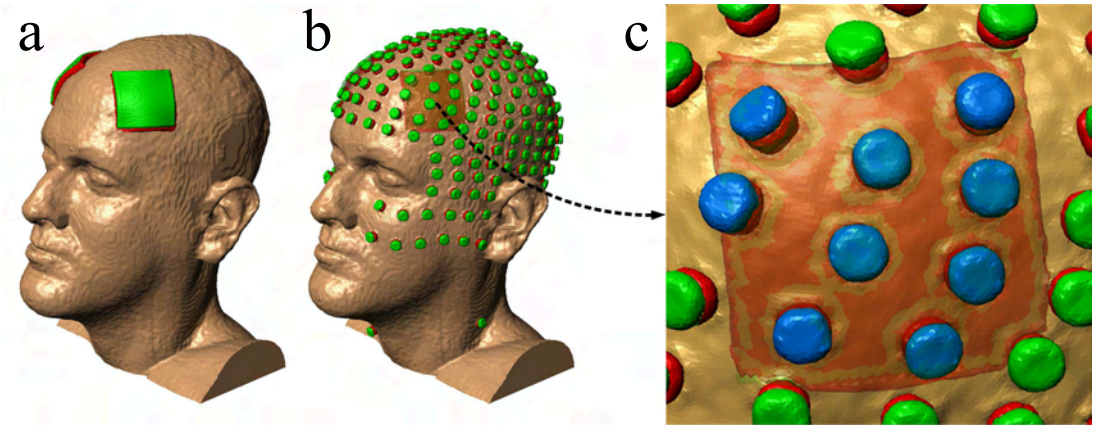

Figure 2.15: Sampling process: (a) Location of the F3-F4 Pad configuration on the head model. (b) Overlay of pad-electrodes used to determine which HD electrodes are considered for sampling. (c) Selection of the subset of electrodes (blue) within the pad area used to simulate the pad by linear superposition.

2.3.2 Surface area calculation and normalization

First comparisons between pad solutions and sampled pad solutions showed a strong difference in some cases, meaning a high error (Section 2.4). It took some time to figure out that this was due to a missing "current calibration". The problem here was that in Abaqus only certain current densities (1 A/m^2=1 mA/1000 mm^2) can be set, not the actual current. As the surface areas of the electrodes differ due to smoothing in the meshing process, a scaling to 1 mA total current injection per electrode becomes necessary.

To calculate the exact areas of the discretized electrode surfaces, first only the surface elements and nodes of the volume mesh have to be determined (Matlab function "freeBoundary.m"). As the current density in Abaqus only relates to the surface area with "air-contact" it is necessary to distinguish between electrode surface and the directly connected gel surface.
The energized area is the difference of the total electrode surface area and the intersection between electrode and gel surface areas (Figure 2.16).

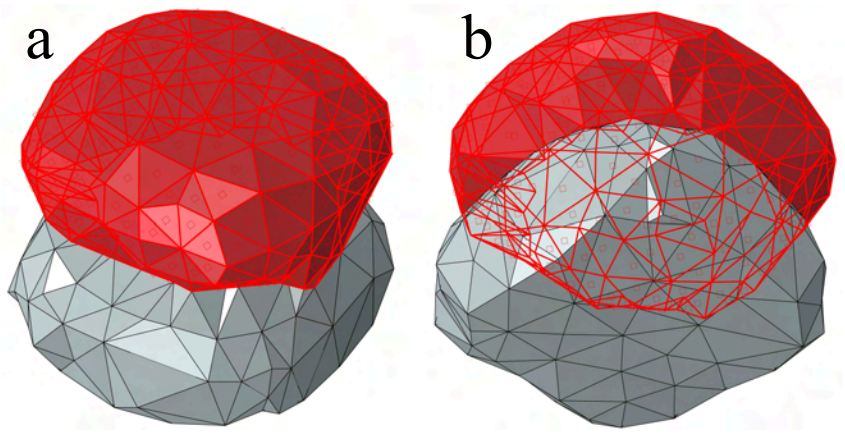

Figure 2.16: Tetrahedral mesh of a single HD electrode (4 mm radius) shown from (a) above and (b) below. Only the red colored surface accords to the energized area. Gray surface shows the gel layer.

After identifying the energized nodes and elements, the energized area can be calculated as the sum of all surface areas of n faces (simple triangle $\mathbf{ABC}$):

$$energized\ area = \frac{1}{2} \cdot \sum_{i=1}^{n} |\overrightarrow{AB}_i \times \overrightarrow{AC}_i|, \tag{2.2}$$

where the vectors $\overrightarrow{AB}$ and $\overrightarrow{AC}$ point respectively from $\mathbf{A}$ to $\mathbf{B}$ and from $\mathbf{A}$ to $\mathbf{C}$.

Energized surface areas of the HD electrodes (4 mm radius) are in the range of 110-150 mm^2. These variations are mainly caused by the smoothing algorithms during the mesh generation and the electrodes' orientation on the scalp. Corresponding areas of pad-electrodes (5 $\times$ 5 cm^2) are about 2700-3300 mm^2. Having calculated all specific surface areas of each electrode, the solutions were scaled by multiplying each with the corresponding factor: $\frac{1000}{\text{energized area in mm}^2}$

2.3.3 Electrode weight distribution

Simulations show that current density distribution on a continuous pad is not uniform. To explore whether emulating such an uneven distribution on the array could improve performance, 3 different methods of distributing current among the subset of HD electrodes were tested(uniform, non-uniform, and optimal):

Uniform distribution

The simplest approach is a uniform weighting whereby every single electrode is set to the same current intensity value (Figure 2.17a).

Non-uniform distribution

In a continuous pad, currents are not uniformly distributed (see Figure 2.17e). To emulate this behavior 3 simplified non-even distributions of currents on the available subset of electrodes (Figure 2.17b-d) were tested. Electrodes were defined as corner, border or center electrodes depending on their distance from the center of the pad (corner: outside of outer ellipse, center: inside the inner ellipse, border: between the two ellipses; the axes of the outer ellipse are given by the pad dimensions and the axes of the inner ellipse are 75% from these values (Figure 2.17e)). Ellipses are used since also rectangular pad electrodes were tested (for squared pads the ellipses can be represented by circles). The following weightings of current density for corner-border-center were tested: 3-2-2 (Figure 2.17b), 6-3-2 (Figure 2.17c) and 15-5-2 (Figure 2.17d). The uniform distribution can be represented by the weights 1-1-1.

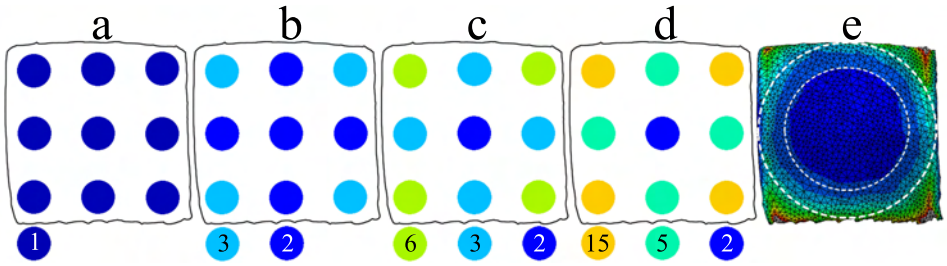

Figure 2.17: (a) uniform distribution, (b-d) different weights for electrode positions and (a) the continuous pad solution with the 3 regions "corner", "border" and "center".

Optimal distribution

Since the solutions for the continuous pads are available, also a best-case solution can be computed. This is done by optimizing the weightings using least-squares optimization, which were constrained to have correct signs and to add up to a total of zero current (i.e. electrodes in a pad are either cathodal or anodal and all current entering must also exit the head). This can be implemented with linearly constraint least-squares [23]:

$$\mathbf{s}_{\text{ls}} = \arg\min_{\mathbf{s}} \|\mathbf{E} \cdot \mathbf{s} - \mathbf{p}\|^2 \text{ subject to } s_i > 0,\ s_j < 0 \text{ and } \mathbf{s}^T \cdot \mathbf{1} = 0, \tag{2.3}$$

where $\mathbf{E}$ is the matrix with the electrode's solutions used to sample the pad, $\mathbf{p}$ is the actual pad solution arranged as a vector and $\mathbf{s}$ are the weighting factors for each electrode which are to be optimized. i, j indicate the index of the anodal and cathodal electrodes, respectively.

The optimal weightings among the electrodes seem to be arbitrary, so that there is no rule of thumb deducible which generally applies to all configurations (Figure 2.18).

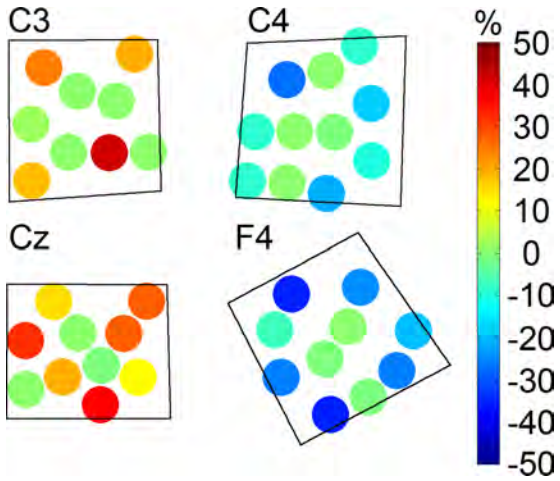

Figure 2.18: Example of optimal weight distributions for the 2 configurations C3-C4 and Cz-F4. Colors indicate the percentage of each electrode of the total current distribution (positive for anodes and negative for cathodes). There is no general pattern observable, even though it seems that electrodes at the border generally might have a higher weight.

2.4 Error calculation

2.4.1 Magnitude error

The solutions for the pad and sampled pad were compared in terms of field magnitude and location of peak stimulation, which is perhaps a more relevant criterion for clinical applications. The electric fields obtained for the continuous pad and sampled are denoted by $\mathbf{E_p}$ and $\mathbf{E_s}$, respectively. With these the relative error is defined as:

$$e_{\text{rel}}{}^2 = \frac{\|\mathbf{E_p} - \mathbf{E_s}\|^2}{\|\mathbf{E_p}\|^2}, \tag{2.4}$$

where $\| \quad \|^2$ denotes the square sum over voxels and xyz-dimensions of the field vector. The calculation of relative errors was performed for gray and white matter voxels separately.

2.4.2 Location error

Areas of peak intensity (voxels in the brain with electric field intensities in the upper quartile) were compared using the Jaccard index:

$$J(P_p, P_s) = \frac{|P_p \cap P_s|}{|P_p \cup P_s|}. \tag{2.5}$$

P_p, P_s are the peak masks from pad and sampled pad results, respectively. A Jaccard index close to 1 indicates high overlap while an index close to 0 denotes no overlap.

3 Results

The idea is, to use the linearity of the Laplace equation to simulate a single pad-electrode with a linear superposition of smaller electrodes. Two important questions arise in this context: How accurately do the resulting electric fields with this sampled solution replicate the fields obtained with the continuous pad-electrodes? Furthermore, how should one distribute the current among the subset of HD electrodes to achieve a faithful replication of the continuous pad-electrodes? To answer these questions 10 standard pad configurations were simulated. Here, the results of a comparison of the current distributions between the continuous pad-electrodes and the sampled pads are presented.

3.1 Comparison between continuous and sampled pads

3.1.1 Intensity is generally accurate with an average error of 5%

The results for field magnitude are exemplified for one pad configuration in Figure 3.1 showing a good correspondence of the sampled pad with the continuous pad.

To quantify the difference, the relative error (Equation 2.4) for all configurations was calculated (Figure 3.2), using different possible weightings among the subset of sampling electrodes (Figure 2.17). The entire list of error values is attached in the appended Table A.1.

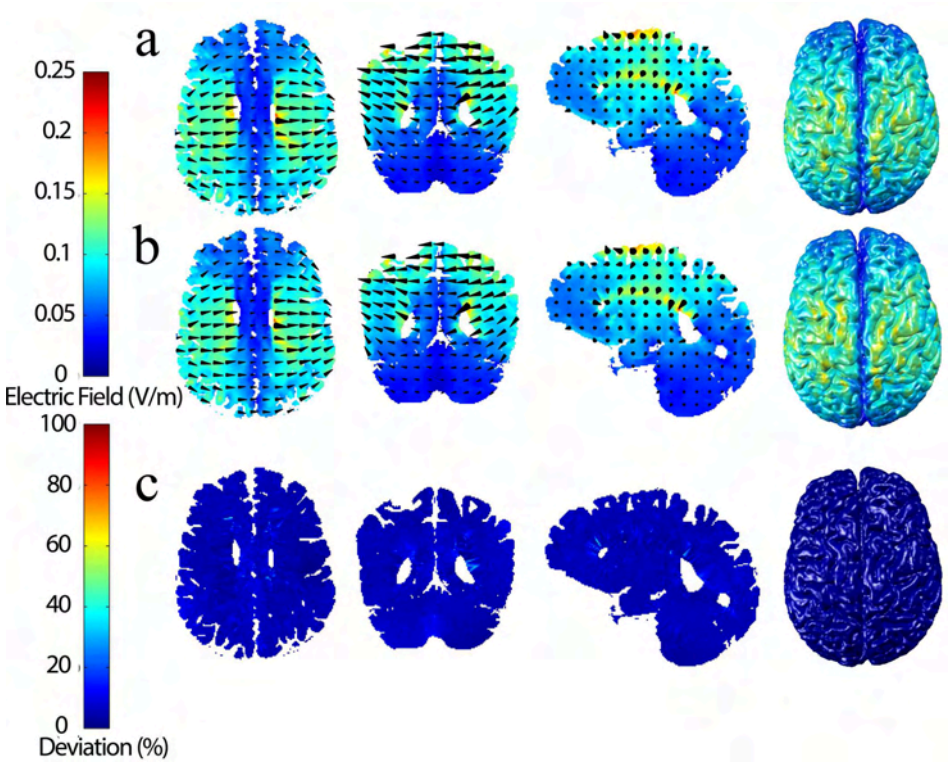

Figure 3.1: Electric field distributions for (a) continuous pad, (b) sampled pad and (c) their difference, acquired for the pad configuration C3-C4 using the uniform distribution. There is no visible difference between (a) and (b), resulting in a very small error (c).

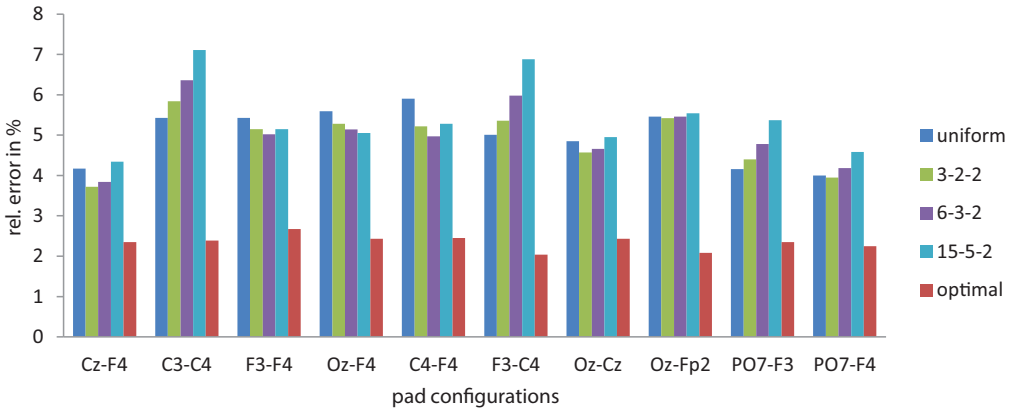

Figure 3.2: Error rates for all pad configurations and the different sampling methods for GM tissue.

With a uniform current distribution the relative error in field magnitude is $5\% \pm 0.68\%$ for GM and $4.62\% \pm 0.7\%$ for WM (mean $\pm$ std across 10 pad configurations). Other current distributions give similar results with the exception of the optimal solutions, as expected, as it uses additional information (Figure 3.3, Section 3.2).

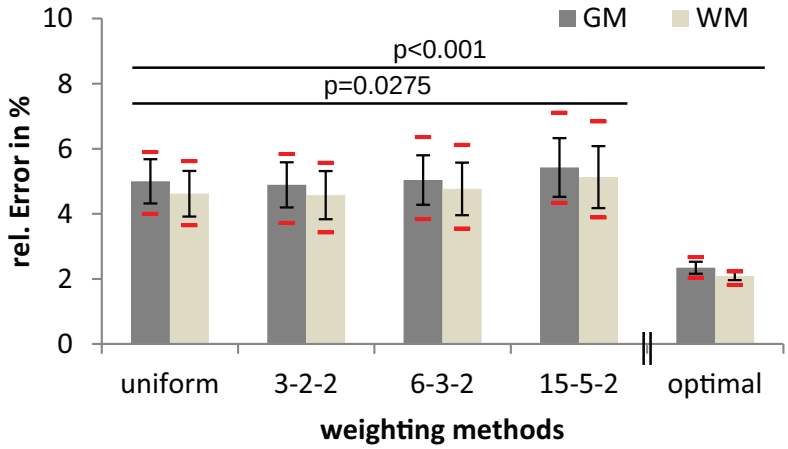

Figure 3.3: Error rates averaged across all pad configurations for the different sampling methods (black error bars indicate the standard deviation across configurations, red bars indicate the minimum and maximum errors). P-values indicate results from repeated measures ANOVA and paired t-test respectively (see Section 3.2)

The 3-2-2-weighting results in an average error of $4.89\% \pm 0.69\%$ for GM and $4.58\% \pm 0.74\%$ for WM. The errors for 6-3-2- and 15-5-2-weightings are $5.04\% \pm 0.76\%$ for GM and $4.77\% \pm 0.81\%$ for WM and $5.43\% \pm 0.9\%$ for GM and $5.13\% \pm 0.95\%$ for WM, respectively. The optimal current distribution leads to an average error of $2.34\% \pm 0.18\%$ for GM and $2.09\% \pm 0.13\%$ for WM.

3.1.2 Accuracy of peak intensity location is around 94%

To determine the locations of maximal stimulation and whether they differ significantly for the sampled solution, the Jaccard index (Equation 2.5) comparing areas of peak field intensity (top 25%) was calculated. Results indicate a very good overlap with a Jaccard index of $94.28\% \pm 2.03\%$ (Figure 3.5) using the uniform distribution. Similar results are obtained using the 3-2-2-, 6-3-2- and 15-5-2-weightings with average indices of $94.48\% \pm 1.98\%$, $94.56\% \pm 1.91\%$, $94.17\% \pm 1.69\%$, respectively. The uniform distribution again outperforms with an average index of $96.35\% \pm 1.28\%$.

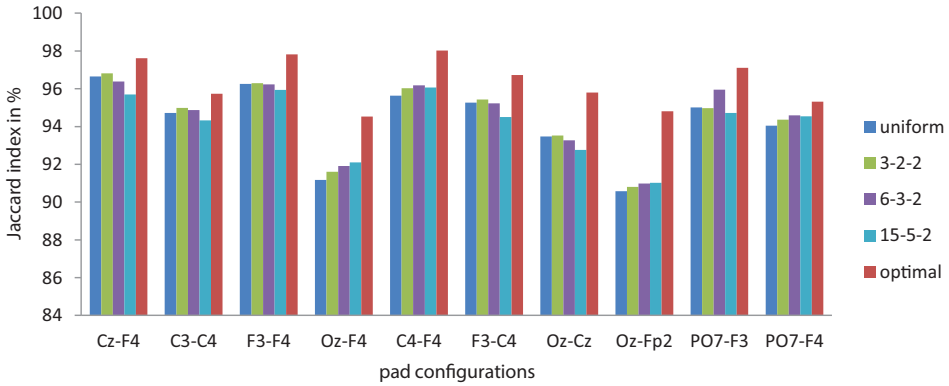

Figure 3.4: Jaccard indices for all pad configurations and the different sampling methods indicating the change in locations of the peak (top 25%) electric fields for GM tissue.

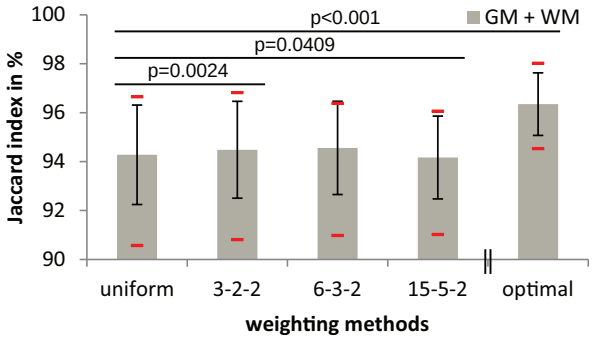

Figure 3.5: Jaccard indices averaged across all pad configurations for the different sampling methods.

3.1.3 Sampled region requires complete coverage

The 10 different pad configurations are all comparable in terms of errors, which are in the range of 4-6% (Figure 3.7a). A major determinant for the adequacy of this sampling approach is a complete coverage of the pad with the sampling electrodes. An example of this problem is shown in Figure 3.6a where partial coverage leads to substantially higher error in field magnitude (Figure 3.7a) and a lower Jaccard index for peak intensity (Figure 3.7b).

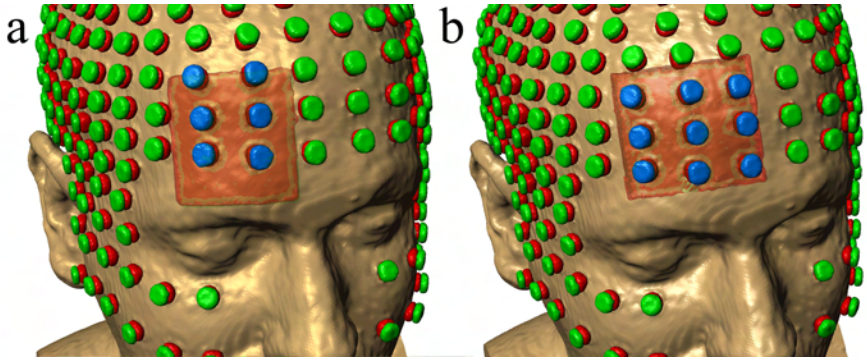

Figure 3.6: (a) Pad FP2 with an insufficient sampling coverage and (b) a well sampled pad.

The field magnitude error between continuous and sampled pads for the configuration Oz-Fp2 is $5.47\% \pm 0.505\%$, whereas for the insufficient sampled pad Oz-Fp2* the error is $10.125\% \pm 0.174\%$. Similar results can be observed for the peak intensity locations, where the Jaccard Indices are at $90.85\% \pm 0.21\%$ and $85.22\% \pm 0.13\%$ respectively (Figure 3.7b).

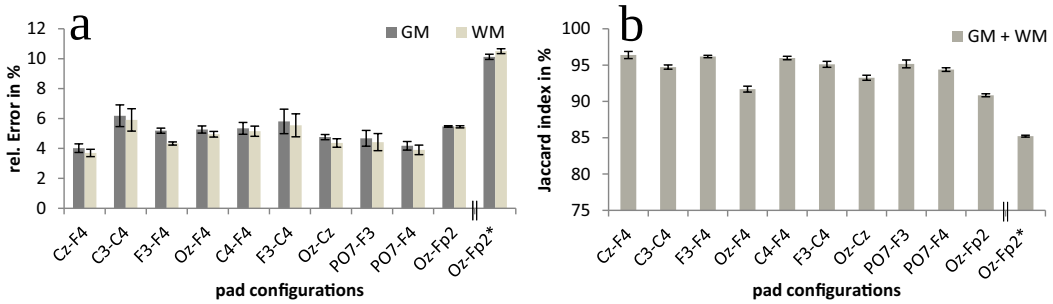

Figure 3.7: (a) Error rates and (b) peak intensity Jaccard indices averaged across all weighting methods. Oz-Fp2* and Oz-Fp2 correspond to figures 3.6a and 3.6b respectively.

3.1.4 Additional results

Error calculation for different tissue types

The relative error calculation for different tissue types, using the uniform distribution among the HD electrodes, reveals an increasing error for tissues that are closer to the electrodes (Figure 3.8 and Figure 3.9). This is an expected outcome: as one moves further away of the electrodes the blurring of current distributions (primarily at skin/bone and CSF/bone boundaries) reduces the effect of discrete sampling on the surface.

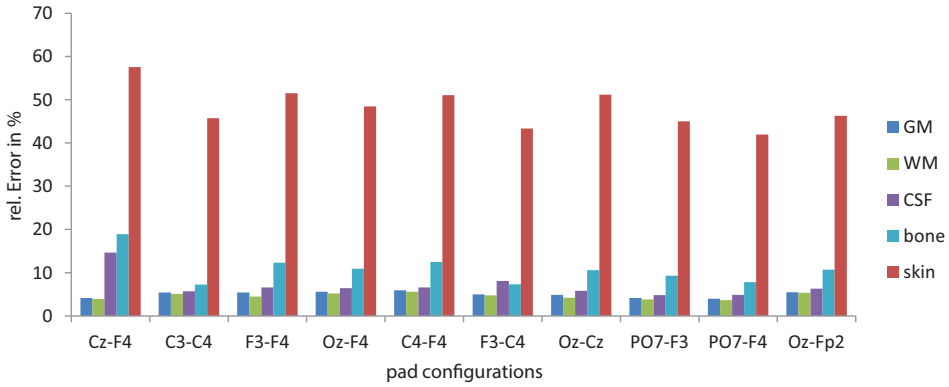

Figure 3.8: Error rates for all pad configurations for the different tissue types based on a uniform weighting among the HD electrodes.

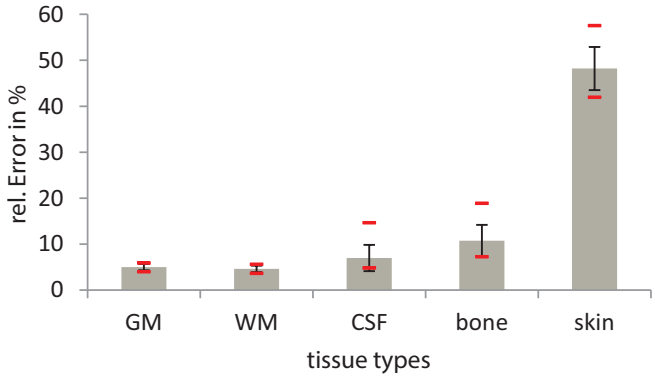

Figure 3.9: Error rates averaged across all pad configurations for the different tissue types based on a uniform weighting among the HD electrodes.

The Jaccard indices for the different tissue types, also using the uniform distribution, show an increasing overlap of peak intensity locations for tissues that are closer to the electrodes (Figure 3.10 and Figure 3.11). Again, this is expected as the sampling has been selected precisely to overlap in area, while at a distance the blurring of current flow may lead to a reduced overlap.

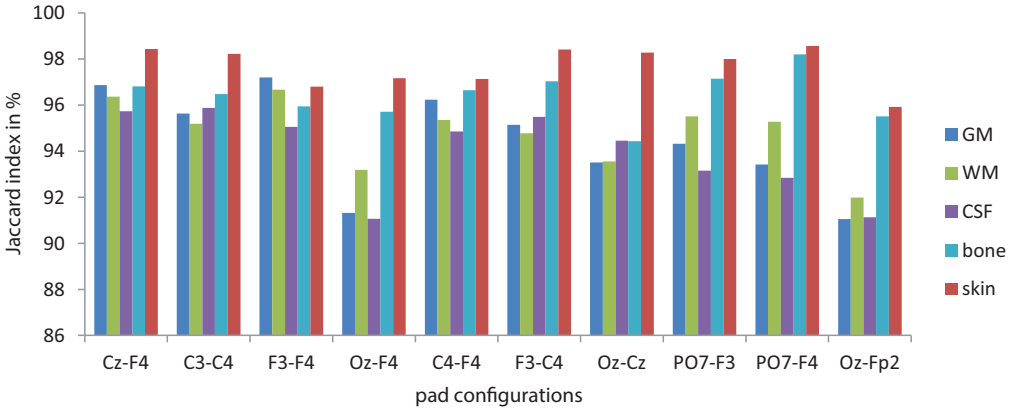

Figure 3.10: Jaccard indices for all pad configurations for the different tissue types based on a uniform weighting among the HD electrodes.

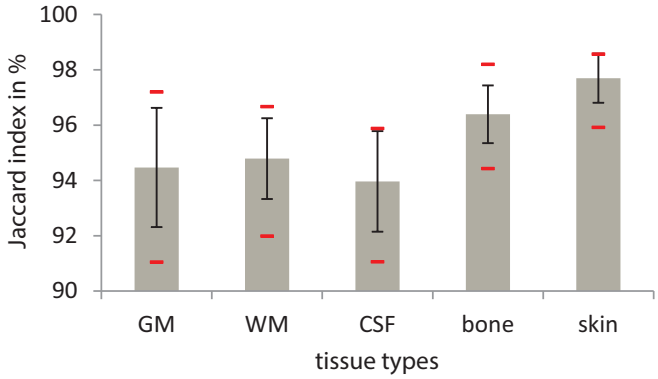

Figure 3.11: Jaccard indices averaged across all pad configurations for the different tissue types based on a uniform weighting among the HD electrodes.

Analysis of the HD electrode array resolution

To investigate the necessary resolution of HD electrodes, the error rates for different amounts of electrodes used for sampling were computed. Starting with 2 HD electrodes (one for each pad) more electrodes were added incrementally. In each step the relative error and locations of peak intensity overlap were calculated. Electrodes were selected at random, so this evaluation was repeated 100 times per configuration to obtain a mean behavior with increasing electrode counts. The analysis is based on the uniform weighting and for GM only. An analysis of the error behavior for different HD electrodes resolutions reveals the following:

Increasing the number of HD electrodes leads to a decreasing relative error (Figure 3.12a) and an increasing Jaccard index, indicating a higher overlap of peak intensity areas (Figure 3.12b). One should use caution when extrapolating this data: These simulations used a constant electrode size, and in addition, as the number of electrodes increases the spacial overlap of the set of electrodes with the exact shape of the pad improves.

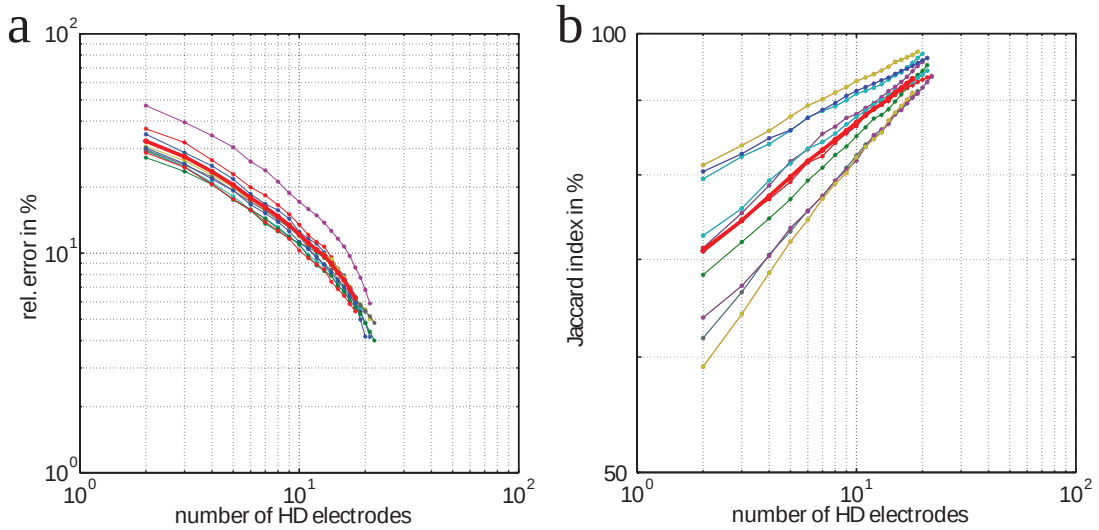

Figure 3.12: (a) Error rates and (b) Jaccard indices averaged over 100 runs of adding random electrodes for the 10 different pad configurations based on a uniform weighting for the GM tissue. Thick red line indicates the average over the 10 configurations.

3.2 Non-uniform current distribution

To determine if the different methods of distributing currents among the sample electrodes differ, a repeated-measures one-way analysis of variances (ANOVA) with 5 conditions (uniform distribution, 3-2-2-, 6-3-2-, 15-5-2-weighting and optimal distribution) was performed. A significance level of 5% was considered for all hypothesis tests.

The test showed a significant difference (probability value $p = 2.2 \times 10^{-16}$) between the various methods. Obviously, the optimal solution outperforms the others, since it uses the pad solution as a prior information. Inspection of these optimal solutions reveals that they are not readily predictable and thus this performance cannot be trivially achieved in practice. Leaving out the optimal solution and conducting an ANOVA for the 4 remaining methods still results in a significant difference ($p = 0.0275$). A comparison of the mean values shows that the 15-5-2-weighting produces the highest error and leads to this test result. Pairwise t-tests reveal that there is no significant difference between uniform and 3-2-2-weighting ($p = 0.36$), 6-3-2-weighting ($p = 0.85$) and 15-5-2-weighting ($p = 0.17$). Comparable results were obtained for the white matter tissue.

In summary, none of the tested weight-distributions outperforms the naïve uniform distribution.

3.3 Software implementation

To practically use the technique proposed in this thesis the existing software HDExplore by Soterix Medical Inc. (Figure 1.5) was further developed. For this the model with 332 electrode solutions (without 4 neck electrodes) was integrated. The MRI and the solution files had to be cropped to smaller dimensions and changed in orientation to follow given visualization standards. I added new controls, as f.e. selecting arbitrary anodal and cathodal HD electrodes and distributing the current uniformly among these electrodes (Figure 3.13).

Also the user now is able to select predefined sampled pads (Figure 3.14) and investigate the field distribution for all possible pad configurations (Figure 3.15).

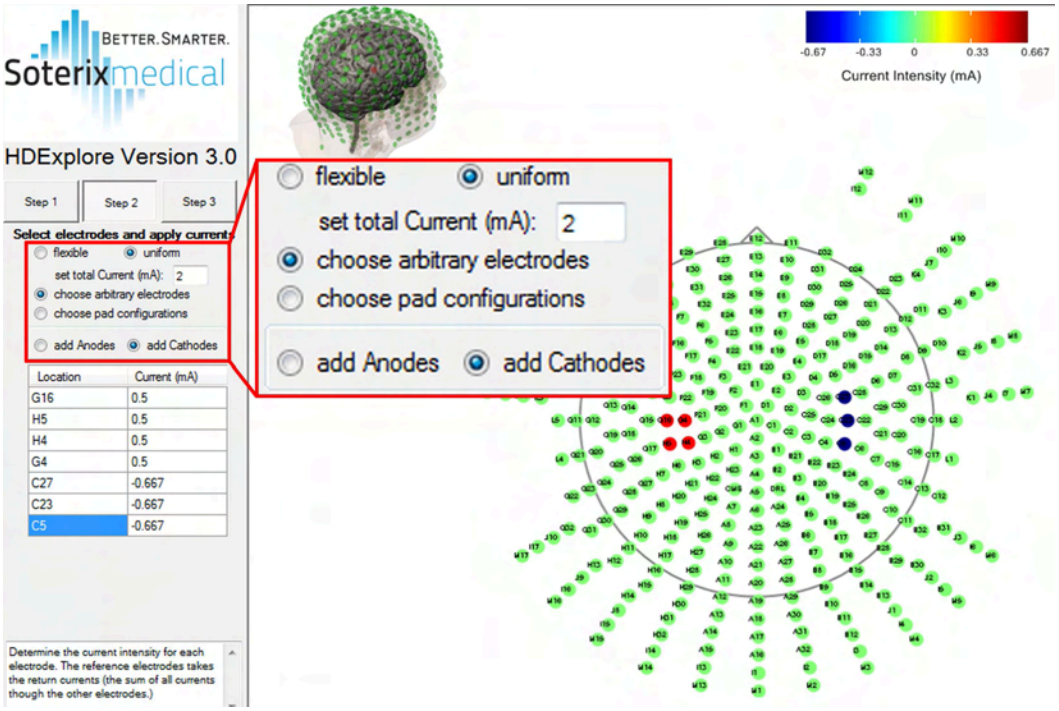

Figure 3.13: New version of the software HDExplore (Soterix Medical) including the 332 HD electrodes model. Detail shows new controls to add specific electrodes. The current is then automatically distributed uniformly among the selected electrodes.

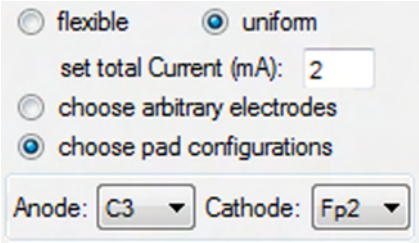

Figure 3.14: Controls to select predefined pad-electrodes to be sampled with HD electrodes.

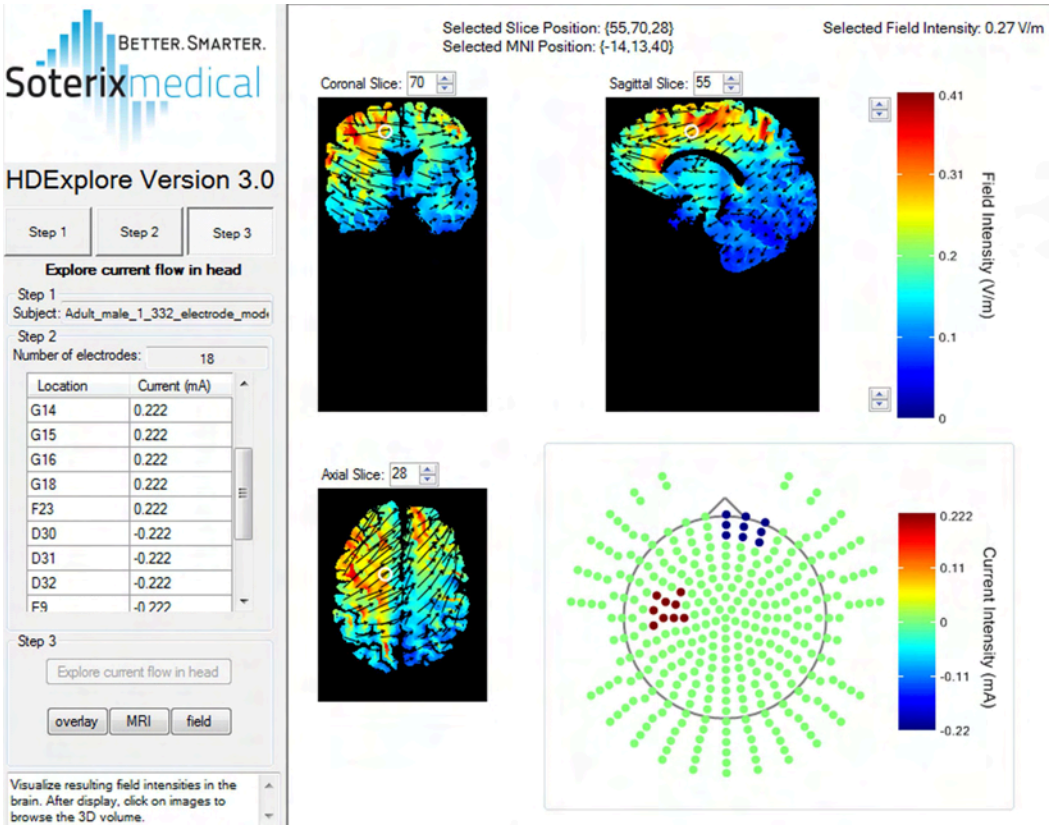

Figure 3.15: Field distribution for the pad configuration C3-Fp2 sampled with HD electrodes.

4 Conclusion

Transcranial Direct Current Stimulation (tDCS) is a non-invasive neuromodulation technology that is under investigation as a treatment for a variety of neurological conditions. Today, sponge-electrode pads are commonly used for current injection in tDCS. Computational models often provide guidance on the placing of these pads by predicting current flow in the brain. The necessary spatial resolution for modeling requires complex specialized software and substantial computational resources, making accurate modeling impractical in clinical setting. To efficiently estimate the current distribution for arbitrary pad configurations, pad-electrodes were simulated with an array of high-definition (HD) electrodes. The simulation of the pad is based on the linear superposition of single precalculated electrode solutions.

Numerical results on 10 different pad configurations show that electric field intensity simulated with the sampled array deviates from the solutions with pads by only 5% and the locations of peak magnitude fields coincide by 94%. Best results are obtained when assuring complete coverage of the electrode pad with sampled electrodes. The precise distribution of currents among the HD electrodes is of minor importance, making the uniform distribution an obvious choice. Pad sampling is expected to become the preferred approach for individualized treatment and current targeting in clinical research.

Currently the computation and preparation time needed to evaluate a specific electrode configuration is approximately 6 hours for an experienced technician in a specialized laboratory and assuming segmented head models are already available. In contrast, a two part process is desired: Step 1 evaluates the FEM model with high-end computers and software to precompute solutions for each HD electrode in the array. In Step 2 practitioners use a "thin" client to quickly explore different electrode configurations.

With this approach the initial calculation of FEM solutions (Step 1) would still require approximately 1 hour per electrode. This computationally demanding step would not happen at the site of the end-user, which typically will not have access to such specialized software and hardware. Instead this computations would be performed where such expertise resides, i.e. at a university laboratory or commercial company. Additional expertise needed for this Step 1 is the segmentation of the high resolution MRI, which is not feasible in a clinical setting (radiologists do not have the time for detailed segmentation of the entire head anatomy, and automated techniques are still in development).

However, Step 2 can readily be implemented on a low-end computational platform at the site of the end-user. This step takes no more than 2 minutes on a typical desktop computer (5 seconds per electrode, with 20.3 ± 1.34 electrodes for the configurations tested here). With standard heads, the expensive Step 1 is performed only once and Step 2 is executed by many different clinical researchers that have varying targets and electrode configurations in mind.

Evidently performance would increase with increasing electrode count (Figure 3.12) but one should use caution in extrapolating this data. Regardless, it is evident that increasing the number of electrodes provides diminishing returns and a 6% error is within the variance that is expected from different modeling choices. So further increasing electrode counts may not be justified based on the current state of the art in current flow modeling.

A corresponding graphical user interface that uses this sampling approach has been developed (Figure 3.15). Further development regarding this project might be the advancement of the modeling pipeline. Future projects are f.e. to further investigate the quality of freeware tools to generate FEM meshes or the FEM computation itself with the aim to finally automate the whole pipeline with the help of freeware.

The approach presented here also allows for the use of anisotropic current density models (based on diffusion tensor imaging (DTI)), which might be implemented in future work as well. Also this model could be used for targeting (HDTargets by Soterix Medical Inc.), where the optimal HD electrodes configuration and current for a specific stimulation are determined automatically. For this the already existing optimization algorithm [23] needs to be applied on this model.

Bibliography

[1] M A Nitsche and W Paulus. Excitability changes induced in the human motor cortex by weak transcranial direct current stimulation. *The Journal of physiology*, 527 Pt 3:633–639, September 2000. PMID: 10990547.

[2] M. A. Nitsche, L. G. Cohen, E. M. Wassermann, A. Priori, N. Lang, A. Antal, W. Paulus, F. Hummel, P. S. Boggio, F. Fregni, and A. Pascual-Leone. Transcranial direct current stimulation: State of the art 2008. *Brain Stimul*, 1(3):206–223, Jul 2008.

[3] Abhishek Datta, Varun Bansal, Julian Diaz, Jinal Patel, Davide Reato, and Marom Bikson. Gyri -precise head model of transcranial DC stimulation: Improved spatial focality using a ring electrode versus conventional rectangular pad. *Brain stimulation*, 2(4):201–207, October 2009. PMID: 20648973 PMCID: PMC2790295.

[4] Abhishek Datta, Marom Bikson, and Felipe Fregni. Transcranial direct current stimulation in patients with skull defects and skull plates: high-resolution computational FEM study of factors altering cortical current flow. *NeuroImage*, 52(4):1268–1278, October 2010. PMID: 20435146.

[5] Preet Minhas, Marom Bikson, Adam J Woods, Alyssa R Rosen, and Sudha K Kessler. Transcranial direct current stimulation in pediatric brain: a computational modeling study. *Conference proceedings: ... Annual International Conference of the IEEE Engineering in Medicine and Biology Society. IEEE Engineering in Medicine and Biology Society. Conference*, 2012:859–862, 2012. PMID: 23366028.

[6] Mirko Windhoff, Alexander Opitz, and Axel Thielscher. Electric field calculations in brain stimulation based on finite elements: An optimized processing

pipeline for the generation and usage of accurate individual head models. *Human Brain Mapping*, 34(4):923–935, 2013.

[7] Yu Huang, Jacek Dmochowski, Yuzhuo Su, Abhishek Datta, Christopher Rorden, and Lucas C Parra. Automated MRI segmentation for individualized modeling of current flow in the human head. *Journal of Neural Engineering*, 2013. Submitted.

[8] Chang-Hwan Im, Ji-Hye Park, Miseon Shim, Won Hyuk Chang, and Yun-Hee Kim. Evaluation of local electric fields generated by transcranial direct current stimulation with an extracephalic reference electrode based on realistic 3D body modeling. *Physics in medicine and biology*, 57(8):2137–2150, April 2012. PMID: 22452936.

[9] Moritz Dannhauer, Benjamin Lanfer, Carsten H Wolters, and Thomas R Knoesche. Modeling of the human skull in EEG source analysis. *Human brain mapping*, 32(9):1383–1399, September 2011. PMID: 20690140.

[10] David Ames Wells. *The Science of Common Things: A Familiar Explanation of the First Principles of Physical Science for Schools, Families, and Young Students*. Ulan Press, August 2012.

[11] Felipe Fregni, Sigride Thome-Souza, Michael A Nitsche, Steven D Freedman, Kette D Valente, and Alvaro Pascual-Leone. A controlled clinical trial of cathodal DC polarization in patients with refractory epilepsy. *Epilepsia*, 47(2):335–342, February 2006. PMID: 16499758.

[12] Felipe Fregni, Rafaela Gimenes, Angela C Valle, Merari J L Ferreira, Renata R Rocha, Luane Natalle, Riviane Bravo, Sergio P Rigonatti, Steven D Freedman, Michael A Nitsche, Alvaro Pascual-Leone, and Paulo S Boggio. A randomized, sham-controlled, proof of principle study of transcranial direct current stimulation for the treatment of pain in fibromyalgia. *Arthritis and rheumatism*, 54(12):3988–3998, December 2006. PMID: 17133529.

[13] Colleen K Loo, Angelo Alonzo, Donel Martin, Philip B Mitchell, Veronica Galvez, and Perminder Sachdev. Transcranial direct current stimulation for depression:

3-week, randomised, sham-controlled trial. *The British journal of psychiatry: the journal of mental science*, 200(1):52–59, January 2012. PMID: 22215866.

[14] Paulo Sergio Boggio, Roberta Ferrucci, Francesca Mameli, DÃ©bora Martins, Oscar Martins, Maurizio Vergari, Laura Tadini, Elio Scarpini, Felipe Fregni, and Alberto Priori. Prolonged visual memory enhancement after direct current stimulation in alzheimer's disease. *Brain stimulation*, 5(3):223–230, July 2012. PMID: 21840288.

[15] David H Benninger, Mikhail Lomarev, Grisel Lopez, Eric M Wassermann, Xiaobai Li, Elaine Considine, and Mark Hallett. Transcranial direct current stimulation for the treatment of parkinson's disease. *Journal of neurology, neurosurgery, and psychiatry*, 81(10):1105–1111, October 2010. PMID: 20870863.

[16] Julie M Baker, Chris Rorden, and Julius Fridriksson. Using transcranial direct-current stimulation to treat stroke patients with aphasia. *Stroke; a journal of cerebral circulation*, 41(6):1229–1236, June 2010. PMID: 20395612.

[17] Friedhelm Hummel, Pablo Celnik, Pascal Giraux, Agnes Floel, Wan-Hsun Wu, Christian Gerloff, and Leonardo G. Cohen. Effects of non-invasive cortical stimulation on skilled motor function in chronic stroke. *Brain*, 128(3):490–499, January 2005. PMID: 15634731.

[18] Gottfried Schlaug, Vijay Renga, and Dinesh Nair. Transcranial direct current stimulation in stroke recovery. *Archives of neurology*, 65(12):1571–1576, December 2008. PMID: 19064743.

[19] M B Iyer, U Mattu, J Grafman, M Lomarev, S Sato, and E M Wassermann. Safety and cognitive effect of frontal DC brain polarization in healthy individuals. *Neurology*, 64(5):872–875, March 2005. PMID: 15753425.

[20] Tim Wagner, Felipe Fregni, Shirley Fecteau, Alan Grodzinsky, Markus Zahn, and Alvaro Pascual-Leone. Transcranial direct current stimulation: a computer-based human model study. *NeuroImage*, 35(3):1113–1124, April 2007. PMID: 17337213.

[21] Robert Oostenveld and Peter Praamstra. The five percent electrode system for high-resolution EEG and ERP measurements. *Clinical Neurophysiology*, 112(4):713–719, April 2001.

[22] Phan Luu, Zhongqing Jiang, Catherine Poulsen, Chelsea Mattson, Anne Smith, and Don M. Tucker. Learning and the development of contexts for action. *Frontiers in Human Neuroscience*, 5, December 2011. PMID: 22163216 PMCID: PMC3234498.

[23] Jacek P Dmochowski, Abhishek Datta, Marom Bikson, Yuzhuo Su, and Lucas C Parra. Optimized multi-electrode stimulation increases focality and intensity at target. *Journal of neural engineering*, 8(4):046011, August 2011. PMID: 21659696.

[24] R. Lindenberg, V. Renga, L. L. Zhu, D. Nair, and G. Schlaug. Bihemispheric brain stimulation facilitates motor recovery in chronic stroke patients. *Neurology*, 75(24):2176–2184, Dec 2010.

[25] A. Antal, N. Kriener, N. Lang, K. Boros, and W. Paulus. Cathodal transcranial direct current stimulation of the visual cortex in the prophylactic treatment of migraine. *Cephalalgia*, 31(7):820–828, May 2011.

A Appendix

Pad configurations and the HD electrodes used to sample these pads:

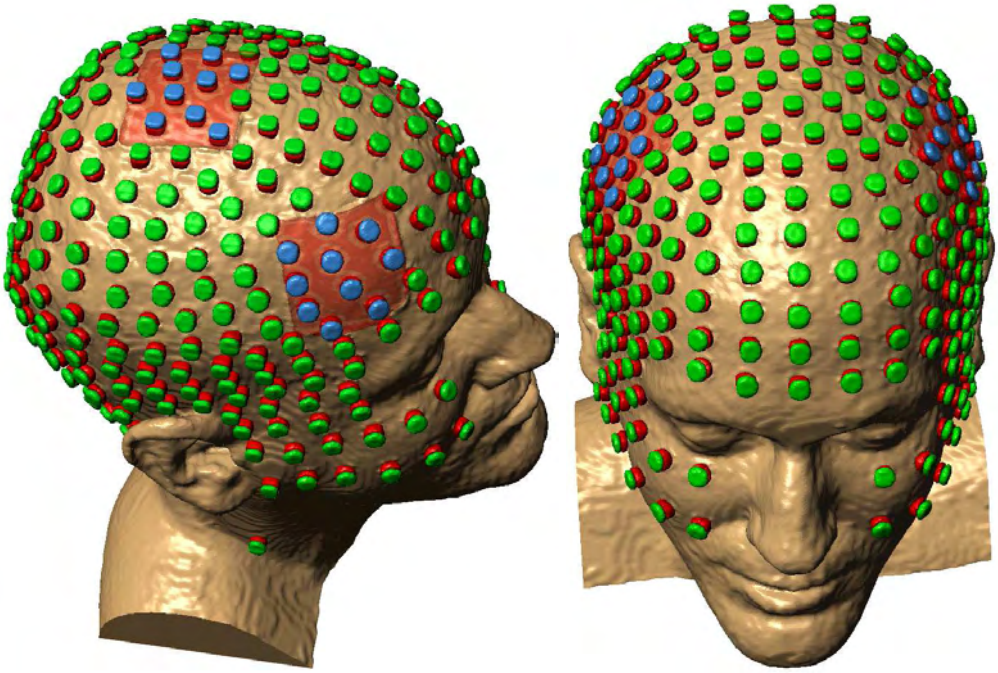

(a) (b)

Figure A.1: (a) Cz-F4, (b) C3-C4. (continued on next pages)

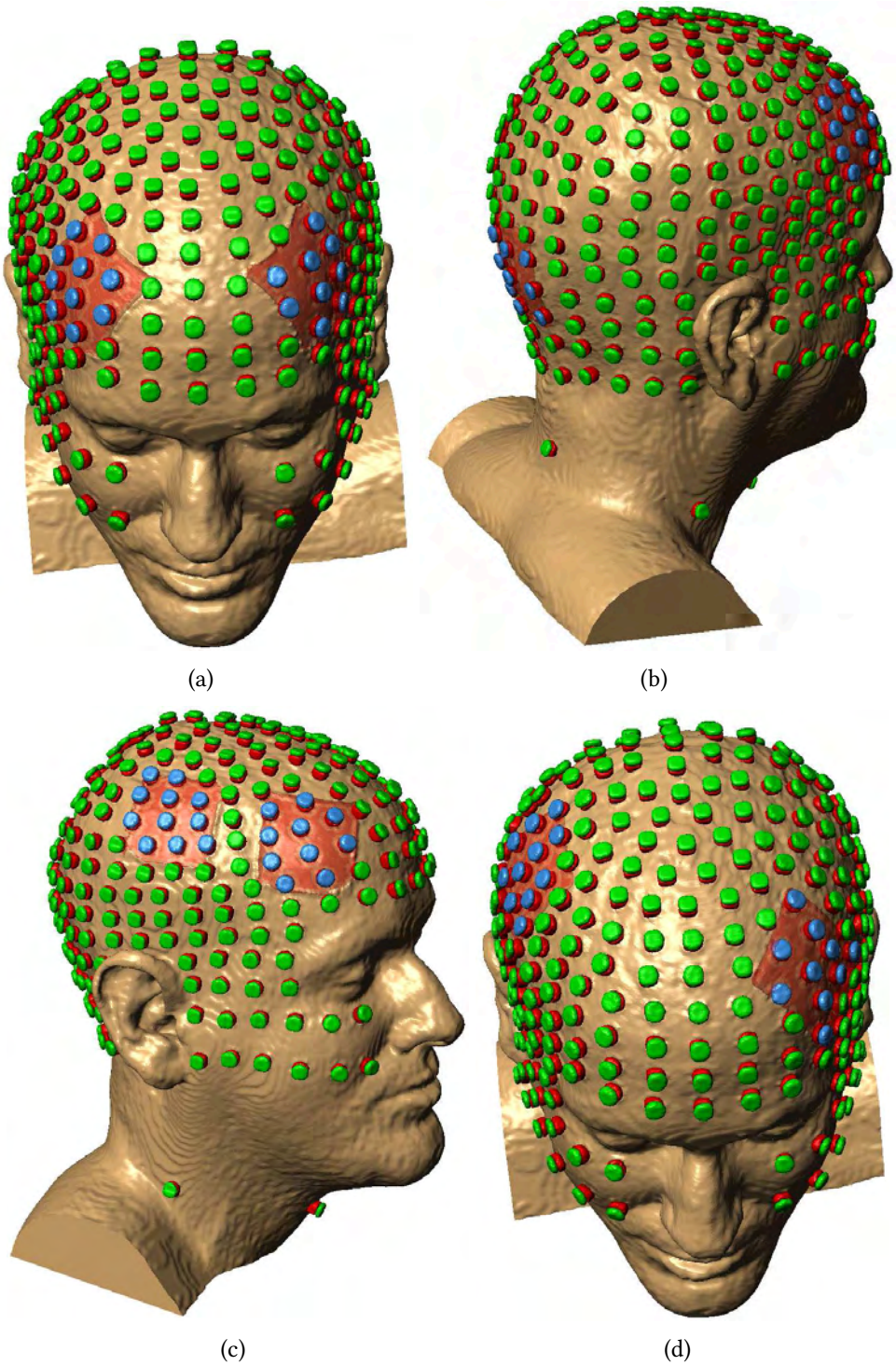

(a) (b)

(c) (d)

Figure A.2: From (a) to (d): F3-F4, Oz-F4, C4-F4, F3-C4.

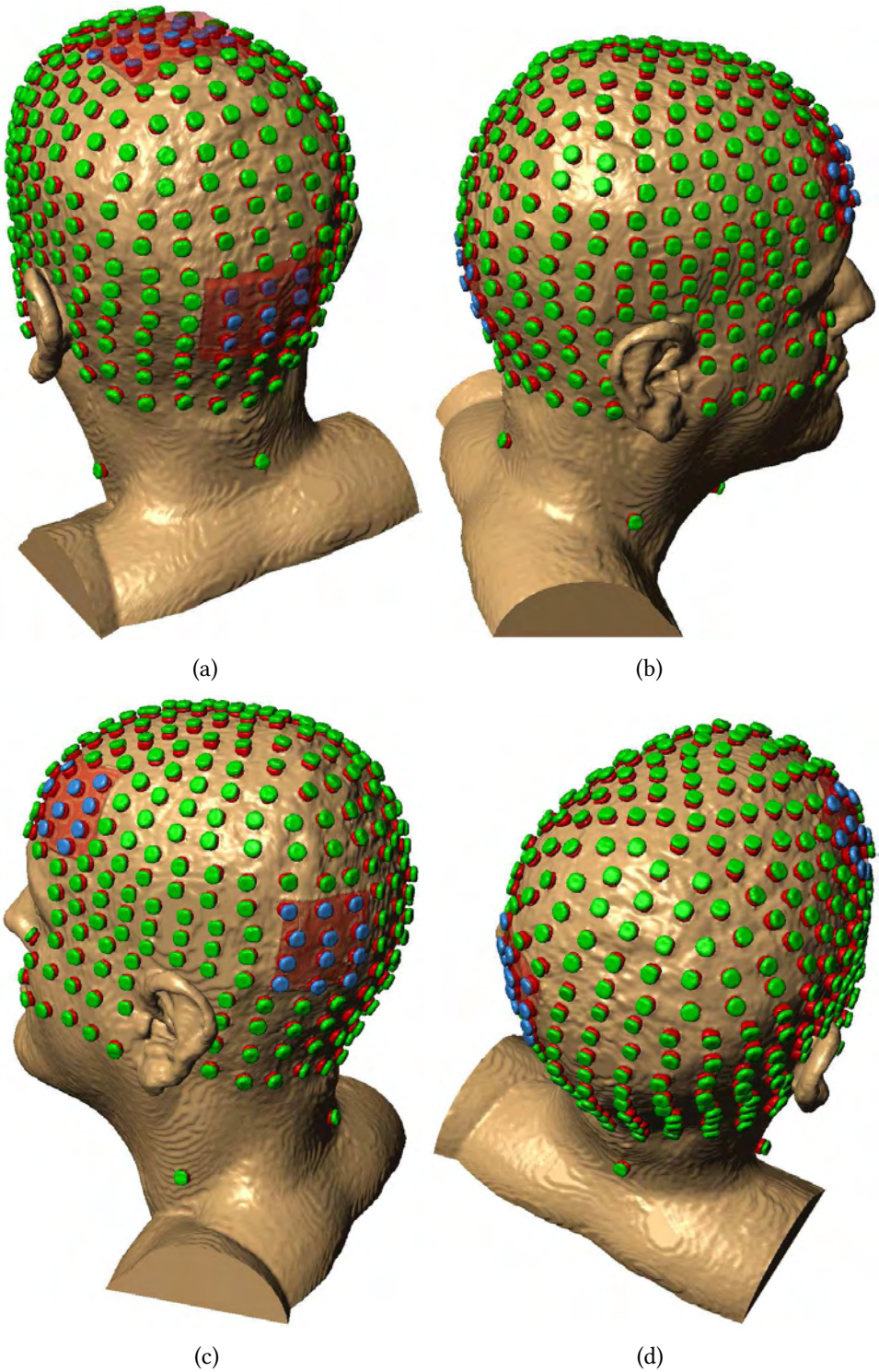

(a) (b)

(c) (d)

Figure A.3: From (a) to (d): Oz-Cz, Oz-Fp2, Po7-F3, Po7-F4.

Table A.1: Field magnitude errors and location of peak intensity comparison between continuous and sampled pads for 10 different configurations (blue values indicate the configuration Oz-Fp2 using the unsufficient sampling coverage (Figure 3.6a)

#	pad configuration	tissue	field magnitude error					location of peak intensity				
			uniform	3-2-2	6-3-2	15-5-2	optimal	uniform	3-2-2	6-3-2	15-5-2	optimal
1	Cz-F4	gray matter	4.17	3.72	3.84	4.34	2.35	96.65	96.82	96.38	95.7	97.62
		white matter	3.92	3.43	3.55	3.89	2.03					
2	C3-C4	gray matter	5.43	5.84	6.36	7.11	2.39	94.72	94.99	94.87	94.33	95.73
		white matter	5.1	5.57	6.12	6.84	2.08					
3	F3-F4	gray matter	5.43	5.15	5.02	5.15	2.67	96.26	96.3	96.23	95.94	97.82
		white matter	4.48	4.3	4.24	4.3	2.13					
4	Oz-F4	gray matter	5.59	5.28	5.14	5.05	2.43	91.17	91.6	91.91	92.1	94.53
		white matter	5.21	4.96	4.85	4.78	2.23					
5	C4-F4	gray matter	5.9	5.22	4.97	5.28	2.45	95.63	96.03	96.18	96.06	98.02
		white matter	5.62	5.01	4.82	5.16	2.1					
6	F3-C4	gray matter	5.01	5.36	5.98	6.88	2.04	95.26	95.43	95.23	94.5	96.73
		white matter	4.76	5.16	5.73	6.53	1.82					
7	Oz-Cz	gray matter	4.85	4.57	4.66	4.95	2.43	93.47	93.53	93.27	92.76	95.8
		white matter	4.22	4.11	4.37	4.76	2.23					
8	PO7-F3	gray matter	4.16	4.4	4.78	5.37	2.35	95.01	94.97	95.95	94.72	97.11
		white matter	3.83	4.14	4.57	5.15	2.21					
9	PO7-F4	gray matter	4	3.95	4.18	4.58	2.25	94.04	94.36	94.59	94.54	95.32
		white matter	3.65	3.68	3.95	4.34	2.09					
10	Oz-Fp2	gray matter	5.46	5.42	5.46	5.54	2.08	90.57	90.81	90.98	91.02	94.81
		white matter	5.39	5.39	5.46	5.54	1.98					
11	Oz-Fp2*	gray matter	10.35	10.16	10.05	9.94	2.97	85.03	85.24	85.29	85.31	93.85
		white matter	10.71	10.54	10.43	10.33	2.55					

I, René Kempe, hereby declare that this thesis and the work reported herein was composed by and originated entirely from me. Information derived from the published and unpublished work of others has been acknowledged in the text and sources are given in the list of references.

Hamburg, 26. August 2013 René Kempe